Princeton Plasma Physics Laboratory

PPPL- 5006

PPPL- 5006

The Physics Basis For An Advanced Physics And Advanced Technology Tokamak Power Plant Configuration, ARIES-ACT1

Charles E. Kessel, et. al.

MARCH, 2014

PPPL PRINCETON PLASMA PHYSICS LABORATORY

Prepared for the U.S. Department of Energy under Contract DE-AC02-09CH11466.

Princeton Plasma Physics Laboratory
Report Disclaimers

Full Legal Disclaimer

Trademark Disclaimer

PPPL Report Availability

Princeton Plasma Physics Laboratory:

http://www.pppl.gov/techreports.cfm

Office of Scientific and Technical Information (OSTI):

http://www.osti.gov/bridge

Related Links:

U.S. Department of Energy

Office of Scientific and Technical Information

Fusion Links

The physics basis for an advanced physics and advanced technology tokamak power plant configuration, ARIES-ACT1

C. E. Kessel[1], F. M. Poli[1], K. Ghantous[1], N. N. Gorelenkov[1], M. E. Rensink[2], T. D. Rognlien[2], P. B. Snyder[3], H. St. John[3], A. D. Turnbull[3]
[1]*Princeton Plasma Physics Laboratory*
[2]*Lawrence Livermore National Laboratory*
[3]*General Atomics*

Abstract
The advanced physics and advanced technology tokamak power plant ARIES-ACT1 has a major radius of 6.25 m at aspect ratio of 4.0, toroidal field of 6.0 T, strong shaping with elongation of 2.2 and triangularity of 0.63. The broadest pressure cases reached wall stabilized $\beta_N \sim 5.75$, limited by n=3 external kink mode requiring a conducting shell at b/a = 0.3, and requiring plasma rotation, feedback, and or kinetic stabilization. The medium pressure peaking case reached $\beta_N = 5.28$ with $B_T = 6.75$, while the peaked pressure case reaches $\beta_N < 5.15$. Fast particle MHD stability shows that the alpha particles are unstable, but this leads to redistribution to larger minor radius rather than loss from the plasma. Edge and divertor plasma modeling show that about 75% of the power to the divertor can be radiated with an ITER-like divertor geometry, while over 95% can be radiated in a stable detached mode with an orthogonal target and wide slot geometry. The bootstrap current fraction is 91% with a q_{95} of 4.5, requiring about ~ 1.1 MA of external current drive. This current is supplied with 5 MW of ICRF/FW and 40 MW of LHCD. EC was examined and is most effective for safety factor control over $\rho \sim$ 0.2-0.6 with 20 MW. The pedestal density is $\sim 0.9 \times 10^{20}$ /m^3 and the temperature is ~ 4.4 keV. The H_{98} factor is 1.65, $n/n_{Gr} = 1.0$, and the net power to LH threshold power is 2.8-3.0 in the flattop.

I. Introduction

It is useful to characterize tokamak power-plant studies in terms of two general parameters indicating the separate levels of confidence in the plasma physics operating regime and in the technology performance of system components. The advanced physics and advanced technology tokamak configuration was last examined in 1999, and referred to as ARIES-AT.[1,2] The preceding study ARIES-RS[3] examined in 1996 also addressed an advanced physics option, with less advanced technology. This corner of parameter space is revisited in light of progress in physics understanding since that time. Future studies will address the conservative corner and the other corners that mix advanced and conservative aspects. The plasma shape is chosen to be strong, preserving the up-down symmetric double-null, which allows higher beta limits in the presence of a stabilizing shell, and plasma rotation, feedback or kinetic stabilization effects. The plasma elongation is 2.2 and triangularity is 0.625. The triangularity is lower than ARIES-AT in order to accommodate neutron shielding on the inboard side and divertor slot design within manifolding and other neutron shielding constraints. The aspect ratio is assumed to be 4.0, based on previous analysis showing this to be a weakly influential parameter between 3.0 and 5.0.[3] The major radius of the plasma has increased to bring the peak

outboard divertor heat flux to < 15 MW/m^2. In addition, the wall-plug efficiency for all heating and current drive systems has been reduced from 0.7 to 0.4, and other recirculating electrical requirements have been increased, which contributes to a larger major radius as well. Time-dependent free-boundary transport simulations and high fidelity heating and current drive analysis are used to confirm the plasma configurations identified with the systems code, and are found to be ideal MHD stable. The pedestal is included consistently by utilizing peeling-ballooning theory to constrain this pressure. The free-boundary simulations have clarified the volt-second requirements needed to assist rampup to steady state, and have shown it is possible to grow a plasma inside the relative tight fitting plasma chamber. Increased attention has been paid to the scrape-off layer and divertor plasma solutions, as well as examining the heat loading associated with steady, transient and off-normal environments. Fast particle stability is examined to determine if instabilities lead to particle losses or redistribution. Discussions of topics including operation at the Greenwald limit, ELM avoidance and mitigation, and tritium burnup are given.

II. Systems Identification of Physics Operating Point

The systems code[4] utilized by the project solves for a 0D plasma power and particle balance, including plasma radiation, and current drive and bootstrap current, along with a series of engineering assessments (first wall and divertor heat flux, neutronic build, TF coil, PF coil, thermal conversion and plant power balance) to determine an operating point's viability. Ultimately the power plant configuration is constructed around the plasma and its cost is determined. The method used is a database approach, where several parameters are scanned to produce a large database of physics configurations, which are subsequently analyzed through the engineering and inboard radial build assessments. For the advanced plasma configurations the β_N is scanned from 4 to 6%, plasma gain Q from 20 to 45, toroidal field from 4.5 to 7.5 T, q_{95} from 3.25 to 6.0, n/n_{Gr} from 0.8 to 1.05, argon impurity fraction from 0.2 to 0.3%, and major radius from 4.75 to 7.5 m. Fixed parameters in the systems scan are plasma aspect ratio at 4.0, triangularity at 0.575, elongation at 2.1 (shape parameters at actual free-boundary separatrix are 0.625 and 2.2, respectively), density profile peak to volume average at 1.3, temperature peak to volume average at 2.0, τ_p^*/τ_E of 5.0, current drive (CD) efficiency in the plasma of 0.15 MA/m^2-MW (based on 1.5D analysis) at a normalized minor radius of 0.85 to represent the dominant lower hybrid CD source. These scan ranges and fixed parameters are determined by initially running several scoping evaluations with the systems code. A large number of viable physics operating points are established that satisfy the balance equations. These points are then run through the engineering module, the power core is built around the plasma, cost determined and filtered to provide 1000 MW electric power operating points. The filters used, apart from 1000 MW electric, were $n/n_{Gr} \leq 1.0$, $\beta_N^{th} + \beta_N^{fast} \leq 5.75$, $H_{98} \leq 1.65$, and $q_{div}^{peak} \leq 15$ MW/m^2. The point with the lowest cost of electricity (COE) is determined, and then points with COEs not exceeding 1.05 times the COE_{min} are retained. These remaining points are reordered and a combination of the lowest major radius and the lowest divertor heating cases is chosen with a COE that is 3 mills above the lowest COE point. There remains a large number of operating points

with a range of parameters within the 1.05 x COE_{min} space and this will be discussed in a future publication.

The temperature and density profiles in the systems analysis are given by, where ρ is a normalized minor radius (r/a),

$$n(\rho) = n(0)[(1 - f_n)(1 - \rho^2)^{\alpha_n} + f_n]$$

$$T(\rho) = T(0)[(1 - f_T)(1 - \rho^2)^{\alpha_T} + f_T]$$

Since the systems analysis does not represent the plasma as accurately as a 1.5D analysis, it is necessary to establish input parameters to the systems code that will properly reproduce those from a 1.5D analysis. The exponents and the edge values are adjusted to provide this agreement by comparisons with actual values of central, peak to volume average and edge parameter values. In addition, the plasma volumes are made to agree by using shape parameters at a flux surface slightly less than the separatrix values (e.g. 2.1 for elongation rather than the actual separatrix value of 2.2). The current drive efficiency used in the systems code is made to agree with detailed calculations reported in Sec. VI. Table I shows several parameters from the systems code reference operating point, and 5 cases generated in 1.5D time-dependent analysis with different energy transport assumptions combined with prescribed density magnitude and profile shape.

III. Time-dependent Free Boundary Plasma Simulations

The Tokamak Simulation Code[5] (TSC) is used to simulate the time-dependent evolution of the ARIES-ACT1 plasma from early startup (Ip = 500 kA) to relaxation of the profiles (typically > 2500 s). Five cases are examined, with varying temperature profiles, and two different density profiles. These are described by 1) broad pressure, 2) broad pressure 2, 3) medium (peaking) pressure, 4) peaked pressure, and 5) density with broad pressure (more distributed density gradient). The plasma begins as a full bore plasma, limited on the inboard wall, at a plasma current of 500 kA, and is grown (primarily vertically) to full size and shape over the course of 100-150 s. The plasma magnetic divertor X-point forms very early in order to isolate the plasma from the wall and allow the injection of heating and current drive power. Fig. 1 shows a fully relaxed flattop plasma configuration for the broad pressure case, while Fig. 2 shows a few time slices during the growth and current rampup phase. Also shown are the primary toroidally continuous conducting structures, which are comprised of the tungsten stabilizer plates, the steel ring structure, and the steel vacuum vessel, in order beginning from closest to the plasma, described in more detail in Ref. 6. The poloidal field coils will be discussed in section V. Figs. 3, 4 and 5 show the plasma profiles, plasma current contributions and powers, central temperature, density, internal inductance, and L-H threshold and net powers, for the broad pressure configuration, and are typical of all the cases presented here. Parameters for all 5 cases are given in Table I, and profiles for them are shown in Fig. 6. It is found that the plasma requires ~ 140 V-s to reach full current at 11 MA, and this includes resistive, internal and external inductive contributions. Here it is assumed that 20 Wb are used to bring the plasma to 0.5 MA, giving a total double swing of -80 to +80

Wb. The density profiles are prescribed, and the temperature profiles are given by using an L-mode model[7,8] adjusted for a pedestal. The thermal diffusivity is adjusted through an exponent to provide the peakedness in the temperature profile. In the case of the broad pressure 2, a modification is used in the core to provide a more localized temperature gradient. These diffusivities are globally adjusted to provide sufficient global confinement to reach the desired β level, identified by the systems analysis. The top of the pedestal pressure height is determined by the peeling ballooning model EPED1[9] to be approximately 140 kPa, so that in all cases the $n_{ped} \sim 0.9\text{-}1.0 \times 10^{20}$ /m^3, and the $T_{ped} \sim 4.4$ keV, where we refer to the top of the pedestal. In all cases argon is introduced as the core plasma line radiating impurity at 0.3% of the electron density, although neon was also shown to provide a similar core radiation capability at 0.9% of the electron density. These would be the same impurities introduced in the divertor to obtain a detached operating regime, which is described briefly in Sec. VII, and in more detail in Ref. 10.

Table I. Plasma Parameters for the Systems Analysis Operating Point and 1.5D Analysis

	Sys Op Point	peak p B_T = 7.0 T	med p B_T = 6.75 T	broad p B_T = 6.0 T	broad p 2 B_T = 6.0 T	dens, broad p B_T = 6.0 T
Ip, MA	10.9	11.0	11.1	11.1	11.1	11.0
I_{BS}, MA	9.89	9.49	9.57	9.75	9.20	9.64
I_{LH}, MA	1.04	1.21	1.14	1.12	1.08	1.21
I_{IC}, MA		0.125	0.125	0.125	0.35	0.125
q_{min}, q(0)		2.56, 3.05	2.73, 3.09	2.83, 3.60	2.63, 3.80	2.14, 3.05
li	0.5 (input)	0.60	0.56	0.47	0.51	0.57
n/n_{Gr}	1.0	1.0	1.0	1.0	1.0	1.0
W_{th}, MJ	690	700	687	673	669	638
n(0), /m^3 x10^{20}	1.65	1.67	1.67	1.67	1.67	1.75
$\langle n \rangle_v$, /m^3 x10^{20}	1.3	1.28	1.30	1.33	1.33	1.25
n(0)/<n>	1.27	1.30	1.29	1.27	1.27	1.40
β_N^{th}, β_N^{total}	**4.75, 5.75**	**4.4, 5.15**	**4.45, 5.28**	**4.9, 5.79**	**4.8, 5.67**	**4.6, 5.49**
τ_E, s	2.26	2.25	2.05	1.94	1.95	1.98
$H_{98(y,2)}$	1.65	1.56	1.50	1.50	1.50	1.45
$T_{e,i}(0)$, keV	40.4	54.7, 50.0	46, 41	40, 35.6	38.5,34.4	40.0, 35.6
Te,i(0)/<T>	2.15	2.79, 2.79	2.42, 2.33	2.09,2.05	2.05, 2.0	2.18, 2.13
P_{alpha}, MW	363	382	385	389	389	357
P_{LH}, MW	39	40	40	40	40	40
P_{IC}, MW	3.0	15	15	15	15	15
P_{cycl}, MW	35.0	46	27	23	23	22.0
P_{line}, MW	24.2	36	35	32.7	34.6	29.6
P_{brem}, MW	56.3	46	48	48.4	48.3	44.9
$P_{L\text{-}H,thr}$, MW	109	119	119	119	119	119
$P_{net}/P_{L\text{-}H,thr}$		3.06	2.8	2.86	2.8	2.70
Z_{eff}	2.11	2.0	2.0	2.0	2.0	2.0
n_{He}/n_e	0.097	0.070	0.077	0.076	0.066	0.075
n_{DT}/n_e	0.752	0.79	0.79	0.802	0.82	0.80
n_{Ar}/n_e	0.003	0.003	0.003	0.003	0.003	0.003
High-n stability		U	S	S	S	S
Low-n b/a			0.375	0.30	0.30	0.275

After developing all 5 configurations at the target normalized total beta of ~ 5.75, identified by the systems code, it was found that only the broad pressure cases were stable to high-n ballooning modes near this value, while the medium and high pressure peaking were unstable. The systems analysis had shown that within the low cost of electricity region, there were lower normalized beta solutions with higher toroidal fields that could provide the same electric power. The medium pressure peaking case was modeled again in 1.5D with a normalized thermal beta of 4.45 at a toroidal field of 6.75 T, resulting in a high-n ballooning stable configuration, with larger stabilizing shell location for low-n kink modes. For the high pressure peaking case, it was difficult to find a 1.5D solution at the normalized thermal beta of 4.0 that would generate the fusion power and maintain other constraints, such as the pedestal height. The configuration found has a normalized beta of 4.4 at a toroidal field of 7.0 T, which turned out to still be unstable to high-n ballooning modes. There should also be solutions with broad pressure with reduced normalized beta and a compensating higher toroidal field, therefore operating below their ideal beta limit, but these were not investigated here. The reference case is the broad pressure one noted in the table by shading, although other configurations can be accommodated.

The plasma configurations require global energy confinement improvement over H-mode of ~ 1.5 in order to reach the desired beta values, and these provide > 86% of the plasma current by bootstrap current, the remainder dominated by lower hybrid, which typically drove 1.1-1.25 MA with 40 MW of injected power. Although 15 MW was injected from ICRF for heating and small on-axis seed current, it will be shown in Sec. VI, that only about 5 MW is required in steady state. The core plasma radiation is dominated by bremsstrahlung at about 45-48 MW, while the cyclotron and line losses were about 20-22 and 29-36 MW, respectively. The cyclotron radiation can climb significantly when the profiles become peaked and the toroidal field is high, as in the peaked pressure case. The net power, defined as $P_{net} = P_{alpha} + P_{aux} - P_{rad,core} - dW/dt$, is > 2.7 times the L to H-mode power threshold[11] in the steady flattop. In the simulations the H-mode is initiated at about 100 s when the net power exceeds this threshold. The profiles for the broad pressure case in Fig. 3 show the various heating power densities, parallel current densities, and radiated powers.

Figure 6 shows the safety factor, parallel current density, temperature and density profiles for the 5 cases. In the current density the large bootstrap contribution can be seen, generally centered about $\rho \sim 0.5$, the lower hybrid deposition around $\rho \sim 0.8$-0.9, and the edge bootstrap current (from the pedestal) is suppressed partially by the reverse current lobe from the lower hybrid. The safety factor reflects these current profile shapes, all very flat or reversed. The safety factors are all above 2.0 everywhere, although the minimum q values range from 2.14 to 2.83. The broad pressure 2 case leads to the largest on axis safety factor and strongest reverse shear, since the bootstrap current is concentrated at mid-radius and subsequently drops the most strongly as it approaches the magnetic axis. The more distributed density gradient in the density-broad pressure case causes more bootstrap current at lower minor radius, causing a deeper minimum in the safety factor. The two density profiles examined had their gradient concentrated, and

spread out across the minor radius. It is of interest to compare the resulting profiles with those from predictive transport models although this was not done in this study.

IV. Ideal MHD stability of low-n external kink, high-n ballooning modes, vertical mode, and peeling-ballooning modes

The plasma configurations established by the time-dependent TSC simulations are examined for their ideal MHD stability to low-n external kink modes, high-n ballooning modes, and peeling-ballooning modes. The PEST1[12] code is used for the low-n and the BALMSC[13] code is used for the high-n modes. The JSOLVER[14] fixed boundary flux-coordinate equilibrium solver is used to recalculate and refine the equilibrium before mapping for stability calculations. The plasma characteristics are input to the EPED1[9] peeling-ballooning analysis to determine the range of pedestal pressure heights expected, giving a range of total pedestal pressures as a function of the pedestal density, shown in Fig 7. There is a trend to higher pedestals at higher density since higher collisionality reduces the local bootstrap current and the drive for peeling instabilities. With the density at the pedestal of about 0.9-1.0x10^{20} /m^3 the pedestal temperature is determined to be ~ 4.4 keV. The location of the top of the pedestal is determined to be at a poloidal flux of 0.92. Here we assume that the ion density and temperatures are the same as the electrons at the pedestal. This pedestal pressure range is enforced for all time–dependent and stability analyses.

Three of the plasma configurations from the 1.5D simulations are stable at the $\beta_N^{th}+\beta_N^{fast}$ target of ~5.75, those with the broadest pressure profiles. These are found to be stable to high-n ballooning modes at plasma triangularities of 0.525-0.725. This value of β_N exceeds the no-wall beta limit for low-n kink modes, and therefore requires some stabilizing conducting structure in conjunction with plasma rotation[15,16], feedback control[17,18], and/or kinetic stabilization[19] mechanisms to be stable. The stabilizing structure locations for low-n kink stability, as a function of the plasma triangularity, for toroidal mode numbers 1-5, are shown in Fig. 8, for the broad pressure case. For our plasma triangularity of 0.625, the shell must be located at 0.3 times the minor radius, measured from the plasma boundary. The structures, made of tungsten, are located over the outboard region not occupied by the vertical stability structures, they lie in the middle of the breeding blanket, and are not toroidally continuous. The thickness of this shell is chosen to provide a time constant ($\tau_w \sim \mu_o \Delta b/\eta_w$) of about 0.1 s, to allow for reasonable feedback currents and voltages,[2,16] ending up about 1 cm thick. Normal copper feedback coils for the resistive wall mode, the mode that the external kink mode becomes in the presence of a resistive shell, are located behind the blanket and shield, and are individual window coils on each sector (16 in total). Shown in Fig. 9 are the wall locations versus toroidal mode numbers, for the broad pressure, broad pressure 2, density with broad pressure, and medium pressure peaking cases for triangularity of 0.625, showing similar locations. For the medium pressure case at lower β_N^{total} (= 5.28) the wall location is shifted to higher values and determined by lower toroidal mode numbers.

There are vertical position feedback coils located behind the shield, above and below the midplane, which are normal copper coils, and can be seen in Fig. 1. These work in

conjunction with the dedicated tungsten stabilizing shells located both on the outboard, approximately from 60-90 degrees from plasma geometric center, and the inboard. From previous work on stabilizing shell locations[1] for vertical stability, the plasma elongation of 2.2 requires a shell on the outboard at about 0.33 times the plasma minor radius, measured from the plasma boundary. This achieves a stability factor, $1 + \tau_g/\tau_{L/R}$, of 1.2, which corresponds to a safe resistive wall location. The ratio of conductor shell thickness to resistivity Δ/η for vertical stability is approximately determined to be ~ 1.0×10^5 /ohm, for feedback coils located behind the shield, toroidally continuous shells, and proper poloidal coverage noted above. The shells are a few cm thick, and will be made toroidally continuous by having them traverse radially outward to the back of the shield or ring structure where connections are made. Tungsten is chosen to provide high electrical conductivity along with high temperature operation typical of the ceramic structure blanket.

V. Fast Particle MHD Stability

It is now well known that the features of advanced tokamak plasmas can aggravate fast particle instabilities due to high central ion temperatures and safety factors, in the presence of strong fast particle pressure gradients. In order to study this on the ARIES-ACT1 design, a 1.5D model for fast particle MHD stability[20] based on linear stability analysis, and which is an extension of the critical gradient model developed previously,[21] is applied. The approach is to use the spatially local analytic growth and damping rates for toroidal Alfven eigenmodes (TAEs) for the case of interest. This allows one to construct the critical fast ion beta gradient profile under the assumption that the quasi-linear (QL) diffusion from overlapping resonances is applicable to the energetic particle (EP) profiles in the presence of these modes. The applicability of the 1.5D model requires a large number of such modes to be present, and this is expected in the reactor regime. Similar conditions can be envisioned in ITER-like burning plasmas in a variety of plasma scenarios.[21]

We assume that the critical beta gradient is determined by the following expression,

$$\left.\frac{\partial \beta_{fast}}{\partial \rho}\right|_{crit} = \frac{\gamma_{damp}}{\gamma_L^*}$$

where β_{fast} is the fast particle beta value at the mode position ρ in the absence of quasilinear relaxation, γ_L^* is the linear growth rate in absence of dissipation, and γ_{damp} is the damping rate without the destabilizing source. The linear growth rate is assumed to be of the form $\gamma_L = \gamma_L^* \, \partial\beta_{fast}/\partial\rho$ with γ_L^* taken as independent of the energetic particle beta profile. Hence in the region of the unstable mode we require that the quasilinear relaxation will result in $\partial\beta_{fast}/\partial\rho \leq \partial\beta_{fast}/\partial\rho\big|_{crit}$. If the EP gradient, predicted by TRANSP, is larger than this critical value, then it is relaxed by the 1.5D model to the critical value enabling the prediction of the EP beta gradient profile. The resulting beta gradient is used for the subsequent computations of the fast ion beta profile. Comparing

the relaxed QL beta profile with the initial one enables an evaluation of EP losses as well as other quantities.

The 1.5 D model has an option to improve the accuracy of the expressions for the growth and damping rates by using NOVA-K[22] rather than with analytic estimates. In this option the code TRANSP is used to improve the EP distribution model. With these modifications the model accurately captures the TAE or RSAE (also called Alfven Cascades) eigenfunctions and their stability properties. Normally we make such growth/damping rates normalization at two to four radial points so that the applied growth rate is multiplied by the ratio $\gamma_{NOVA}(r_i)/\gamma_{analytic}(r_i)$, and then a linear interpolation of the normalization factor is used to continuously express the local growth rate over the whole radial domain between locations r_i. The final EP distribution does not resolve the velocity space dependence, as only the pressure profile is relaxed. To account for the velocity space relaxation, rules based on the work of Kolesnichenko are used.[21]

The application of the 1.5D model to some recent DIII-D experiments[23,24] where tangential NBI is used to excite TAE like modes was successful[20,25]. A plasma formed with the reversed magnetic shear created favorable conditions for EP induced AE damping and trapped electron collisions. Notably the trapped electron damping comes from the edge of the plasma whereas the instability drive is peaked near the half of the minor radius. The 1.5D analytic model is relatively easy to apply in the integrated simulations. In the analytic version the 1.5D model relies on the expressions for the TAE stability without time-consuming numerical analysis. It seems to be extremely useful for the future fusion planning exercises where approximate predictions, whose relative values tend to be accurate, can be rescaled and then applied.

We use this approach for the ARIES-ACT1 plasma, shown in Fig. 10. The alpha profile computed initially by TRANSP code, and the relaxed profile are shown, indicating the removal of particle from the core and re-distribution toward the edge. The $T_i(0)$ versus $\beta(0)$ diagram shows the potential variation of the plasma parameters and its effect on the AE stability. It can be seen from this figure that the ARIES plasma is close to experiencing TAE induced alpha losses, however in this case they only lead to redistribution without losses. Future work will examine this behavior in more detail between redistribution and loss for a range of central q, $T_i(0)$, and $\beta(0)$, in order to provide guidance for plasma configuration optimization.

VI. Approaching or Exceeding the Greenwald Density Limit

The Greenwald density limit[26] , $n_{Gr} = Ip/(\pi a^2)$, poses a limitation to the plasma density, generally resulting in a disruption when it is exceeded. The detailed physics behind this process is not understood, although increasing radiation and edge plasma cooling are clearly features in the evolution to the disruption. The collapse appears to start at the plasma edge and can be poloidally localized. Power plant configurations routinely end up at densities close to or even exceeding n_{Gr} in order to provide sufficiently high fusion power, which scales as $n_D n_T$. Energy confinement scalings, such as the IPB98(y,2)[27],

demonstrate an increase in plasma stored energy as the density increases, which further enforces the identification of a configuration at higher density and low confinement multiplier (e.g. H_{98}). A number of tokamak experiments[28-31] have exceeded the Greenwald density by controlling the scrape-off layer density (scrape-off layer pumping) and fueling from neutral beams (central fueling) or pellets rather than from the plasma edge. These experiments have reached n/n_{Gr} values of 1.4 without disruptions and high confinement that is similar or slightly worse than ELMy H-mode ($H_{98} \sim 0.8$-1.0). It is also found that moving the plasma away from nearby solid surfaces[31] or the gas fueling source (more generally any neutral source) can allow this, higher triangularity[32] can maintain high confinement at these densities, and impurity seeding with Ne, Ar, or Si[31] can aid in maintaining the high confinement at high density.

Since pellet fueling is expected to be the most efficient fueling method in the power plant regime, and in ITER, where edge fueling is assumed to be weak due to higher electron density and temperature at the edge, exceeding the Greenwald density may be justified. However, this will have to be made consistent with the high density divertor operation used to radiate the large powers entering the divertor, via the corresponding scrape-off layer density and neutral concentration. Although the ARIES-ACT1 design point assumes a $n/n_{Gr} = 1.0$, it is of interest to examine the impact of densities exceeding the Greenwald value, in particular since it strongly affects the fast particle stability by decreasing $T_i(0)$ as n increases. Shown in Fig. 11 is the result of a scan in the systems code isolating operating points with electric power outputs of 1000 MW_e, divertor peak heat flux < 15 MW/m^2, $\beta_N^{total} < 5.75$, $H_{98} < 1.65$, and $n/n_{Gr} < 1.6$. Although similar results occurred at other plasma major radii, the plotted results are restricted to the ARIES-ACT1 value R = 6.25m. The resulting H_{98} values ranged from 1.6 at $n/n_{Gr} = 1.0$ to 1.2 at $n/n_{Gr} = 1.6$, as noted earlier due to the favorable density scaling in IPB98(y,2). More importantly, the plot shows a significant reduction in the central ion temperature, which is a primary variable affecting fast particle instability. A move from n/n_{Gr} from 1.0 to 1.2 drops the central temperature from > 40 keV to about 27 keV. The fast particle beta is also reported in the figure and shows a similar strong drop with increasing density.

The geometric dependence of the Greenwald limit also has implications for power plants. As the device major radius increases, so does the minor radius, for a fixed aspect ratio. The trend to larger tokamaks in order to relieve the divertor heat loads, as has occurred in the ARIES-ACT1 study relative to the ARIES-AT design, tends to net lower the Greenwald density, making it that much easier to exceed when optimizing fusion power. This can be aggravated by the steady state requirement of 100% non-inductive current, which tends to hold the plasma current down (operate at higher q_{95}) in order to reduce the recirculating power. In spite of various tokamak experiments demonstrating operation above the Greenwald density, it is not common practice to operate in this regime, at least partly due to current drive efficiency or other limitations of the specific installed heating and current drive sources. It will be necessary to demonstrate more routine operation at such densities, and with the corresponding highly radiative divertor and high non-inductive core current drive, in order to gain confidence in these plasmas for the power plant regime.

VII. Poloidal Field Coil Design

The poloidal field (PF) coils must provide the plasma equilibrium force balance and assist in driving inductive current in the current rampup phase. The inboard solenoid coils primarily provide the inductive current drive and the outer PF coils primarily provide the equilibrium, although strictly speaking each coil contributes to both functions. The plasma is found to require ~ 140 V-s of assistance in ramping up the plasma current from 500 kA to 11 MA, with an additional 20 V-s assumed to be lost in breakdown and early startup phases before reaching Ip = 500 kA. Both equilibrium calculations and TSC are used to establish fiducial states where the coil currents are examined in order to determine the best location for the coils. These fiducial states span plasma current from 500 kA to the flattop value of 11 MA, li(1) values from 1.3 to 0.5, β_N values of 0 to 5.75, and flux states from -80 to +80 Wb. The coil locations, sizes, and maximum coil currents are shown in Table II. The coil locations are significantly constrained in terms of their closeness to the plasma by the radial build from first wall, breeding blanket, shield and support, vacuum vessel, TF coil, and TF coil support structures. In addition, the coils are limited in poloidal distribution by supports, manifolding and ductwork. Shown in Fig. 12 is the plasma cross-section and final poloidal field coil distribution. The location of the outermost PF coil is found to have a significant effect on the overall coil stored energy, where moving the coil towards the Z=0 tends to lower the energy, but are constrained by the vacuum vessel port extensions. The coil cross-sections are also listed in Table II, and are determined with an assumed maximum overall coil current density of 15 MA/m^2. The initial magnetization is -80 Wb, and the flattop magnetization is 80 Wb.

Table II. ARIES-ACT1 poloidal field coil parameters.

	R, m	Z, m	ΔR, m	ΔZ, m	$\|I_{max}\|$, MA
CS1	2.75	0.9	0.25	1.8	4.54
CS2	2.75	2.7	0.25	1.8	6.80
PF1	3.23	6.57	0.74	0.74	8.38
PF2	3.91	7.03	0.61	0.61	5.55
PF3	4.58	7.26	0.61	0.61	5.59
PF4	6.39	7.45	0.65	0.65	6.41
PF5	7.13	7.45	0.58	0.58	5.00
PF6	9.25	7.15	0.75	0.75	8.40
PF7	10.78	6.61	0.98	0.98	14.45

VI. Heating and Current Drive Systems

The time-dependent simulations of the plasma configurations utilize lower hybrid (LH) and ion cyclotron radio-frequency (ICRF) heating and current drive (H/CD). These are examined in terms of frequency, spectrum and power to determine the best parameters for the power plant configuration. The systems code identifies heating and current drive powers separately, so they do not have to be equal. The 1.5D analysis determines actual efficiencies for the current drive, which are used to correct assumptions in the systems

analysis if required. Electron cyclotron H/CD is also examined to provide on-axis and near-axis current drive flexibility. Neutral beams were not considered due to the difficulty in providing the geometry necessary for tangential injection and its impact on device maintenance and neutronics.

The LH current drive provides current at the level of ≥ 1 MA in the location of normalized minor radius 0.7-0.9, just outside the main bootstrap current lobe, but inside the pedestal bootstrap current lobe. This gives about 0.028 A/W for these plasma configurations. The Lower Hybrid Simulation Code (LSC)[33] is used to provide a 1D Fokker-Planck ray tracing analysis. The waves are launched from the low field side, at varying poloidal angles to identify the highest current drive efficiency and deepest penetration of the waves. The frequency is 5 GHz, chosen to minimize alpha particle absorption and improve accessibility of the waves, while avoiding very small waveguides. The index of refraction is also varied, to maximize the current drive and distribution, from 1.85-2.25 for the co-Ip lobe of the spectrum, while the cntr-Ip lobe is fixed at -4.0. The weighting of the power launched between these lobes in the launched spectrum is 87% co-Ip and 13% cntr-Ip. The ITER passive-active multi-junction (PAM) launcher concept[34,35] is assumed to be the same launcher concept used here, which obtains co-Ip and cntr-Ip power fractions of ~ 70% and ~ 30%, respectively. The higher values used here are to produce an overall CD enhancement of 1.6x determined from GENRAY/CQL3D 2D Fokker-Planck analysis[36,37] for ITER steady state simulations.[38] Shown in Fig. 13 are a series of current profiles from TSC simulations while varying the LH launch parameters, and a summary of the results over all cases examined is given in Table III. The trend of decreasing current drive efficiency at the lowest $n_{||}$ corresponds to increasing conversion of the slow waves to fast waves, which propagate back to the separatrix and reflect into the plasma with n|| upshifts and subsequent damping close to the separatrix (of the fast waves). The trend of decreasing current drive efficiency at larger $n_{||}$ is due to progressively shallower penetration before reaching full absorption, with the associated lower temperatures. The maximum in driven current occurs at $n_{||}$ ~1.95-2.15. Launching from above the midplane provides the highest current drive per watt and yields deeper penetration of the LH waves, and broader current distributions. It is advantageous for tritium breeding to move the launching structure off the midplane where the neutron flux is highest, since it would occupy the blanket volume from the first wall back to the rear of the shield. Although 80^o provides the highest CD efficiency (A/W), this angle interferes significantly with the tungsten passive plate for vertical stability and the vertical position active feedback coil. Therefore 60^o is chosen as the reference and was used in the time-dependent simulations.

The launching structure was assumed to be a PAM, with maximum power density of 20 MW/m^2 through the waveguide assembly. For this, 2 m^2 are reserved on the first wall for this function, for the total of 40 MW of LH power. An additional area is allocated for mechanical support and cooling structures, to make the total LH footprint 2.85 m^2. The details of the waveguide size, spacing, and arrangement[39], has not been specified, although the envelope provided is considered sufficient.

Table III. Lower hybrid parameter scan and resulting driven current for 40 MW, 5 GHz, P-coIp = 0.87, P-cntrIp = 0.13, for the broad pressure configuration.

$I_{LH,}$ MA	$n_{\|\|} = 1.85$	$n_{\|\|} = 1.95$	$n_{\|\|} = 2.05$	$n_{\|\|} = 2.15$	$n_{\|\|} = 2.25$
$\theta = 80$	1.22	1.35	1.30	1.32	1.25
$\theta = 60$	0.98	0.98	1.12	1.10	1.00
$\theta = 40$	0.85	0.92	1.03	1.04	0.95
$\theta = 0$ deg	0.87	0.90	0.98	0.91	0.90
$\theta = -40$	0.77	0.90	0.95	0.93	0.87
$\theta = -60$	0.87	0.96	0.95	0.90	0.84

ICRF heating and current drive is used to heat ions initially, and then to heat electrons as the plasma temperature rises and magnetic axis moves outward. These waves also drive on-axis current with a relatively narrow distribution when phased to do so. This function is useful for providing a seed current on axis that avoids very high values of the on-axis safety factor. For the toroidal field of 6 T at the plasma major radius (6.25 m), the frequency range of 55-65 MHz was examined to place the 2nd tritium resonance near the geometric center or slightly on the high field side, while avoiding other fuel, thermal helium, fast alpha particle, or impurity resonances. The analysis used the TORIC full wave code[40], with a toroidal mode number of 27, launched from the outboard midplane. In steady state the wave power was absorbed on thermal tritium, amounting to 4% at 65 MHz, and 21% at 55 MHz, with the remaining fraction on electrons. There is no alpha particle, thermal deuterium, or argon absorption at 65 MHz. The 65 MHz also provided the highest CD efficiency of 0.045 A/W, and is the reference for ARIES-ACT1. Shown in Fig. 14 is the absorbed power on electrons, thermal ions, and fast alpha particles over the range of ICRF frequencies of 50-100 MHz. It can clearly be seen why the 2nd deuterium resonance frequency range is avoided due the strong fast alpha absorption. Also shown are the power deposition split as a function of time, and the profiles for power to thermal electrons, thermal ions, and driven current. These calculations were performed on the broad pressure 2 plasma configuration in the TRANSP code[41], with a Fokker Planck treatment of the resonant ions (tritium) and an equivalent Maxwellian for the fast alphas. Although the flattop plasma only requires little power to provide the needed seed current, ~ 5 MW, in the startup phase higher power is used to heat the plasma to the burning state, Fig. 14 showing the power trajectory used, and then it is reduced as the alpha power rises.

The launching structure is taken to be similar to the ITER ICRF multi-strap launcher[42], with a maximum power density through the first wall of 10 MW/m^2. Although more advanced structures have been assumed in the past[43], these are immature technologies and have no demonstrations on existing fusion facilities. The ICRF system is based on 20 MW maximum power to the plasma and requires 2 m^2 for the launching structure. With additional mechanical support and cooling structures, the total area reserved for this is 2.56 m^2.

Electron cyclotron current drive (ECCD) is examined as a means to replace ICRF for on-axis CD, and to provide CD in the region of the plasma $0.2 < \rho < 0.6$, for fine-tuning the

safety factor profile. Neither ICRF at low frequency or LH can access this intermediate radial location. In addition, EC can propagate through vacuum and therefore it has no plasma coupling constraints that both IC and LH do have. The ITER frequency of 170 GHz was used since these sources are being actively pursued[44]. Launchers were examined at the outboard midplane R = 7.92 m, Z = 0.0, +/-0.5 m, and off-midplane at 60^o and 80^o, measured from the plasma geometric center, at the corresponding first wall locations. The poloidal and toroidal steering angles were then scanned to examine the deposition locations and CD efficiency. It is found that the highest CD efficiency is ~ 0.012 A/W, significantly lower than the ICRF fast wave CD on axis, however, the flexibility in deposition location was found to be extensive. These analyses are done with GENRAY[36,37] and do not include momentum conserving effects[45] on electron-electron collisions, that are expected to increase the driven current by ~ 15-25%. Shown in Fig. 15 are the kA/MW CD efficiencies (color code) and deposition locations (labeled contours) as a function of the combination of poloidal and toroidal (azimuthal) steering angles. The midplane launchers at Z = 0, Z = -0.5 m, Z = +0.5 m, and the off-midpane launchers at 60^o and 80^o are shown. Deposition examples taken from the contour plots are given to show the resulting profile widths and location compared to the normalized minor radius.

The reference configuration has 40 MW of LH and 5MW of ICRF in the flattop phase, and here we will examine a configuration that replaces ICRF with ECCD and a configuration that uses ECCD in addition to ICRF. These time-dependent simulations use TORAY[46,47] for the ray-tracing analysis of the EC heating and current drive. Figure 16 shows the safety factor profiles and the IC and EC current density profiles of the three configurations. The ECCD has lower current drive efficiency compared to ICRF and 20 MW of injected power are needed to drive about 200 kA of current. The configuration with EC only uses the equatorial launcher, with the center-launcher used for core deposition and the upper and lower launchers used to broaden the current profile. The steering angles have been chosen to closely reproduce the safety factor profile of the reference configuration. The upper and lower launchers are aiming 5 degrees above and below the midplane, respectively, while the mid-launcher is horizontal. The toroidal angle for all launchers is in the range of 20-30 degrees. The third configuration is still using 5 MW IC for core heating, but adds the equatorial launcher to drive current in the range of ρ = 0.25-0.4 to tailor the q-profile and form magnetic shear profiles monotonically reversed in the core. In this case both the mid and lower launcher are aiming 5 degrees below mid-plane. These cases show the effectiveness of EC for safety factor control, particularly in the region where the other CD sources do not provide deposition. All the plasma parameters are largely preserved across these configurations, although the injected power goes from 45 MW (reference) to 60 MW and to 65 MW, which makes the plasma fusion gain go from 44 to 31 to 29.

The launching structures for EC would be smaller than those required for LH or ICRF, and can likely accommodate a larger power density through the first wall. Examining the ITER design for equatorial launchers[48], the footprint on the first wall and subsequent volume required behind these apertures is larger than the actual exit hole for the EC beam. A placeholder value of 1 m^2 is assumed for 20 MW total power. Although this

would depend on how many EC beams are accommodated, and how the beams are steered to the desired locations. In a power plant the deposition locations in the plasma region may be fixed, simplifying the EC design and minimizing the required flexibility and complexity. On the other hand, if the EC is required to provide control of neo-classical tearing modes, for example, some flexibility in steering would be required.

A number of issues persist for heating and current drive systems in the power plant fusion environment. The parts of these systems near the plasma must be made of radiation resistant materials, such a ferritic steels or tungsten, and the use of common materials like insulators, dielectrics, and copper must be minimized or eliminated. These components must also operate at high temperature since they will penetrate the blanket, and must use similar coolants as the blanket (e.g. helium). The wall-plug efficiencies associated with these various sources hovers around ~ 0.4, since it encompasses the source efficiency, the transmission efficiency, and coupling efficiency to the plasma (for IC and LH), and can be low since incentive to improve the efficiency is a lower priority on present experiments. These structures are also mostly void, and designs that incorporate shielding need to be developed. These are essentially plasma facing components, and will see the same environment as the first wall, so that erosion, redeposition, implantation and tritium retention are all critical areas to address.

VII. Scrape-Off Layer and Divertor Plasma Simulations

The heat-flux to material walls depends on the radial (across flux-surface) power width near the outer midplane magnetic separatrix, the subsequent radial spreading of the power width as the heat flows toward the divertor plates, and the location of the line radiation in the scrape-off-layer (SOL)/divertor regions. The fraction of power that can be radiated, the location of the radiating zone relative to walls, and spatial stability of the zone are all key questions to be answered in the power plant regime. Furthermore, the detailed shape of the divertor walls has an impact on the solutions found. Self-consistent 2D, toroidally symmetric simulations of plasma/neutral fluid transport in the SOL/divertor region are presented that show the spatial location of the highly radiating zones and the corresponding heat-flux profiles on surrounding material surfaces.

The simulations use the UEDGE transport code[49] for plasma and neutrals species. The plasma is described by fluid equations for the ion density, ion velocity along and across the magnetic field, B, and separate ion and electron temperatures (T_i and T_e). Transport along B, termed parallel, follows Braginskii[50] with coefficients being flux limited to a fraction of free-streaming thermal transport as the collisional mean-free path becomes comparable to plasma gradient-scale-lengths. Transport coefficients perpendicular to B, assumed to be dominated by plasma turbulence, are prescribed separately for density, velocity, and temperatures based on fitting present-day experiments as used by the ITER Organization for divertor modeling.[51,52] Cross-field electric and magnetic particle drifts are ignored. The atomic neutrals are also described by a flux-limited fluid model, where for hydrogenic species (50%/50% deuterium/tritium), charge-exchange collisions is a dominant process. The impurity species are described as either a fixed fraction of the hydrogenic ion density with the radiation given by a near coronal equilibrium model[53], or

by evolving the individual charge states of the impurity species within the fluid model and using atomic rate tables for ionization, recombination and line radiation of each charge state.

The domain that is modeled by UEDGE includes a small portion of the pedestal region just inside the magnetic separatrix, the full SOL/divertor regions up to the divertor plates and main-chamber walls. The computational mesh is based on a specific MHD equilibrium, with one coordinate being poloidal magnetic flux surfaces and the second coordinate being a blend of orthogonal surfaces and conformal surfaces near the divertor plate; the chamber walls are assumed conformal to an outer flux surface. Two basic types of divertor-plate configurations are considered, one with highly inward-tilted divertor plates as in ITER shown in Fig. 17, and a second open configuration with the divertor plates normal to the flux surfaces as outlined by the dashed line. The mesh shown has only ½ of the radial mesh points actually used to improve visibility of the mesh structure. For the tilted-plate case, both inner and outer plates begin with a more-than-vertical inward angle and then curve more outward so as to intersect the full width for the SOL. Here the focus is on results for the tilted-plated configuration.

The simulations assume up/down symmetry for this double-null configuration, so only the lower half of the edge region is modeled. The following parameters are used: the core flux-surface boundary is located at a separatrix-normalized poloidal magnetic flux of $\psi_n = 0.96$, the outer wall boundary is at $\psi_n = 1.055$, and the private-flux wall (PFW) boundary is at $\psi_n = 0.985$. The divertor plates are strongly tilted toward the X-point as seen in Fig. 17 with the angle between the separatrix flux-surface and divertor plate being 24° and 34° on the outer and inner plates, respectively. At the inner core-boundary, the plasma density is 1×10^{20} m^{-3} and 160 MW is injected into the lower half equally split between ion and electron channels. The radial diffusivities for particles, parallel momentum, and electron and ion temperature are, respectively, 0.3, 1.0, 0.5, and 0.5, all in units of m^2/s. The recycling of ions into neutrals at the divertor plates and walls is unity. The DT neutral density and particle throughput are controlled by a 20 cm neutral pumping region with an albedo of 0.998 on the PFW on the inner divertor leg and by a 20 kA gas puff source on the PFW on the outer divertor leg representing neutral flow under the PFW region, between inner and outer divertor legs. Heat-flux transmission factors on the plates are 3.5 for ions and 5 for electrons. The impurity species is neon and its density is assumed to be 0.004 times the electron density, which would give an effective charge of $Z_{eff} = 1.4$ if the neon is fully stripped. It is found that a lower concentration of argon can be substituted for the neon. The simulation is run to a steady state.

The neon radiation pattern for the ACT-1 solution is shown in the color contour plot of Fig. 17. The radiation concentrates somewhat outside the separatrix in the SOL part of the divertor leg, with fairly broad poloidal extent in both divertor legs though the logarithmic power scale accentuates the range. Neon radiates most strongly in the $T_e = 10\text{-}40$ eV range, which is a consequence of the self-consistent plasma solution for the partially detached plasma in the regions shown with strong radiation. One issue is the proximity of the radiating zone to the core region and possibly degrading the pedestal

temperature. This solution shows only a small reduction in T_e inside the separatrix, and the radiating zone can be moved away from the X-point by increased particle pumping. The total radiated power (neon plus hydrogen) is 120 MW.

The radiation, together with the plasma flux to surfaces determines the total heat-flux to the plasma-facing components. Fig. 17 shows the heat-flux components to the outer divertor plate. The plasma energy flux component includes electron and ion heat conduction and convection energies as well as the recombination energy released upon their recombination within the plate. The smaller neon and hydrogenic radiation components add to make a total peak value of ~12 MW/m^2. The partially detached plasma profiles (not shown) on the plate have the characteristic peak in density near the left peak in heat flux, while T_e and T_i are ~1 eV in, and to the left of, the density peak but then rise sharply to the 100 eV range to the right of the density peak. The other locations with large heat fluxes are on the PFW below the X-point and on the outer wall where it meets the divertor plate. The heat fluxes to the PFW, also shown, is dominated by neon radiation. The total peak heat flux approaches 2 MW/m^2, while placing this boundary farther from the X-point can reduce the peak value. Near the intersection of the divertor plate and main chamber wall there is a comparable 1.5 MW/m^2 heat flux that has a decay width of ~0.3 m along the chamber wall.

Simulations have also been performed in the second configuration indicated in Fig. 17 with divertor plates orthogonal to magnetic flux surfaces and somewhat wider SOLs. For this configuration, stable, fully detached plasma solutions are found for either a fixed-fraction impurity model as above or for evolution of individual impurity charge-states, again using neon as the impurity. The fully detached solution is characterized by a freestanding ionization front located between the X-point and the divertor plate across the full width of the SOL, as opposed to only the inner portion of the width for the partially detached solution. At the ionization front, T_e and T_i drop precipitously to ~1 eV. At such T_e's, plasma recombination becomes strong, and the plasma heat flux reaching surfaces is substantially reduced, and most of the power injected from the core is radiated by neon. As a result, the peak heat flux on the plasma facing components is reduced by a factor of ~2 or more relative to the partially detached solution described above. The operating range and stability of the fully detached plasma can depend on the details of the divertor geometry, but because its evolution is slow (~1 sec), feedback on gas pumping and puffing may extend its useful range. A full description of this second configuration and its characteristics is complex and will be presented in a separate paper[10].

VII. Heat Flux for Steady State, Transient and Off-Normal Loading

An important area requiring improved definition is that of thermal loading in the divertor and on the first wall, so that engineering designs and their operating spaces can be defined[54]. Detailed plasma simulations are reported in Ref. 10, and briefly summarized in the previous section. Here simpler assessments will be described. The steady heat load in the divertor is complicated by the large uncertainty in the power scrape-off width.[55-58] The transient heat loading can be on long or short time scales relative to the

thermal time constant of the plasma facing structure, the former would be largely due to power changes during operations, while the later can be attributed to edge localized modes (ELMs) or other similar short time-scale periodic bursts from the plasma. Uncertainty arises in the absolute amount of power going to the divertor and the first wall, and in characterizing its footprint on these surfaces. The off-normal events pertain to disruptions, the largest of which are the vertical displacement event and the midplane disruptions. Considerable uncertainty exists in prescribing the disruptions heat loads, their final destination, and their footprint. Here we will use a prescription for transient and off-normal loading developed for ITER,[59] which gives approximate loading characteristics, and we will apply them to the ARIES-ACT1 design.

VII-A. Steady state heat loading

The steady state heat loading is parameterized in terms of a conducted and radiated heat flux on the divertor. The loading to the first wall in steady operation is considered small with the large (> 10 cm) scrape-off distance to the wall. Sufficient alignment of the blanket and divertor sectors (16 in total) is assumed in the ARIES study, to avoid leading edges within assembly tolerances, but is otherwise not addressed here. The physical picture of the divertor formulation is that the power is conducted along field lines into the divertor, within the power scrape-off width, which expands as it approaches the X-point and shrinks lightly as it approaches the divertor target. Some power is also transported across field lines, causing a spreading in the power, but the flux expansion is considered the dominant effect. In addition, the tilt angle between the field line and the target plate provide further expansion. It is assumed that the conduction channel is preserved and as the impurity and plasma density rise in the divertor in order to radiate larger fractions of this power, the power in the conducted channel is depleted, but its geometry is fixed. This is a simplification in order to account for radiation, and maintain a concentrated conducted component, but may not reflect the actual physics processes, which are discussed in Ref. 10. However, results from this 2D SOL plasma and neutrals analysis have shown that when the divertor target coincides with the edge of the radiation front, as shown in Fig. 17, the conducted channel can be seen as an increased heat flux, while if they are separated, then the heat flux drops strongly to levels similar to divertor side wall heat fluxes, which are dominated by radiation. The formulation is given by,

$$q_{div}^{peak}\ (MW/m^2) = P_{SOL}\ f_{vert}\ f_{IB,OB}[\ (1-f_{div,rad})/A_{IB,OB,div,cond} + f_{div,rad}/A_{IB,OB,div,rad}\ ]$$

where P_{SOL} is the scrape-off layer power ($P_\alpha + P_{aux} - P_{rad,core}$), f_{vert} reflects an up-down imbalance between divertors, $f_{IB,OB}$ is the inboard and outboard power split, $f_{div,rad}$ is the fraction of power going to the divertor that is radiated in the divertor, and A's represent the footprint areas where power is absorbed. For the conducted power the power scrape-off width at the outboard midplane is given by[55],

$$\lambda_q\ (m) = 7.25x10^{-2} q_{95}^{0.75} n_u^{0.15}/(P_{SOL}^{0.4} B_T)$$

The conducted power footprint areas can then be given approximately by $2\pi(R-a/2)\,\lambda_q f_\psi f_{tilt}$ for the outboard and $2\pi(R-a)\,\lambda_q f_\psi f_{tilt}$ for the inboard, where f_ψ is the poloidal flux expansion (determined from equilibria), and f_{tilt} is the divertor target tilt angle expansion. These are reasonably accurate for the typical plasma geometries examined in the ARIES studies. The radiated power footprint areas are taken approximately as $2\pi(R-a/2)x(a/2)x2$ on the outboard and $2\pi(R-a)x(a/4)x2$ on the inboard, which includes the dome and sidewalls of the divertor slot. Shown in Fig. 18 is the divertor region with poloidal flux, showing the generic geometry of the ACT1, and previous ARIES tokamak studies.[2,3] For the ACT1 design the alpha power is 360 MW, the auxiliary power is 45 MW, with core radiated power of about 115 MW, giving a SOL power of 290 MW. For 80/20 % split for the outboard and inboard, and 65% of the power to each divertor, an outboard divertor receives 150 MW of power. Assuming a 90% radiated power fraction in the divertor, the peak heat flux on the OB divertor is 13.7 MW/m^2, and 5.4 MW/m^2 on the IB. There is some support for the high radiated power fraction in the divertor from 2D SOL plasma and fluid neutral simulations[10], although the stability and controllability of these solutions requires further work in both modeling and experimental demonstrations. The power scrape-off width at the outboard midplane for this case is ~ 4 mm. Power scrape-off width estimates for ACT1 can range from 0.7 mm[58] to 8.0-20.0 cm[56], which constitutes a significant range where engineering design solutions would be very difficult to relatively straightforward, respectively. Advanced divertor solutions with jet-impingement cooling can provide solutions for the heat fluxes calculated here, and are discussed in more detail in refs (6,60,61,62).

VII-B. Transient heat flux from ELMs

Edge localized modes (ELMs) are very short duration releases of energy from the plasma, which propagate both to the divertor and the first wall. Experiments[63-71] to characterize the ELM heat loading indicate that the time scale and waveform of the power to the divertor goes like a parallel ion transit time ($\tau_{||} = 2\pi R q_{95}/c_{s,ped}$) and with a rise (over ~ $2\tau_{||}$) and a fall-off (over ~ $4\tau_{||}$). For ACT1 parameters, $\tau_{||}$ is about 220 microseconds. Large ELMs and small ELMs show a somewhat different power distribution between the divertor and first wall. ELMs are considered to release their energy only to the outboard side for the DN plasma configurations considered here. It is also assumed that the ELM burns through any radiating zone in the divertor, established in the inter-ELM period, due to its large energy content, and therefore they make a footprint on the divertor that is similar to that for steady state conducted power. It has been observed that large ELMs have a footprint expansion of 4-6 times this area, and small ELMs reach about 1.5 times this area[70,71]. Table IV provides the ELM parameters specified for detailed thermo-mechanical[62] analysis along with estimates made using the semi-infinite theoretical expression for the temperature rise of the material surface,

$$\Delta T_{rise}\ (^oK \text{ or } ^oC) = 2/3\ (2\ \alpha^{1/2}\ \Delta W_{ELM}^{div,rise}) / [\pi^{1/2}\ k\ A_{div,ELM}\ (2\ \tau_{||})^{1/2}],$$

$$= 2/3\ C_{material}\ \Delta W_{ELM}^{div,rise} / A_{div,ELM}\ (2\ \tau_{||})^{1/2}$$

where α is the ratio $k/\rho C_p$, k is the heat conductivity, $\Delta W_{ELM}^{div,rise}$ is the energy reaching the divertor in the rise phase, $A_{div,ELM}$ is the area of deposition on the divertor target which is considered the same as between ELMs or includes an expansion factor, and 2 $\tau_{||}$ is the rise phase time frame. The $C_{material}$ is 62 for tungsten at 1000°C and 85 for ferritic steel at 650°C, for $\Delta W_{ELM}^{div,rise}$ in MJ. SiC is the structural material for the ARIES-ACT1 design, and would therefore constitute the first wall, which has a $C_{material}$ of 83, similar to ferritic steel, so those temperature rises can be used for this material. This temperature difference does not include the effects of melting or evaporation, so that a temperature rise above melting only indicates that melting occurs, but does not represent the actual temperature rise including the effects of heat of fusion or vaporization.

Table IV. Edge localized modes heat loading parameters for thermo-mechanical analysis, with both standard ELM and expanded ELM footprints.

	Large ELM	Large ELM-exp	Small ELM	Small ELM-exp
ΔW_{ELM}, MJ	23.4	23.4	5.9	5.9
f_{ELM}, /s	3.7	3.7	18	18
ΔW_{ELM}^{div}, MJ	7.8	7.8	3.1	3.1
$\Delta W_{ELM}^{div,rise}$, MJ	3.1	3.1	0.6	0.6
$A_{ELM}^{div,OB}$, m^2	1.38	5.52	1.38	2.07
$\Delta t_{ELM,rise}$, ms	0.44	0.44	0.44	0.44
$\Delta t_{ELM,fall}$, ms	0.88	0.88	0.88	0.88
ΔT_W, °C or °K	4360	1090	730	490
ΔW_{ELM}^{FW}, MJ	11.7		3.0	
$A_{ELM,FW}$, m^2	99		99	
ΔT_W, °C or °K	203		17	
$\Delta T_{Fe/SiC}$, °C or °K	278		23	

The energy released in an ELM is determined by correlations developed from experiments as a function of plasma pedestal collisionality or ion transit time. These provide the energy as a fraction of the total energy stored in the pedestal. At the collisionality of the ACT1 plasma, the large ELM can reach 20% of the W_{ped}, while the small ELM reaches about 7% of W_{ped} at the associated ion transit time. These provide the ΔW_{ELM} in Table IV. The stored energy in the pedestal is most accurately determined using the pedestal pressure from EPED1[9] analysis, but also by examining a database fit from ITPA in 2003.[72] The released energy during an ELM has a conductive and a convective part, represented by $3\Delta T_{e,ped} \langle n_{e,ped} \rangle V_{ELM}$ and $3\Delta n_{e,ped} \langle T_{e,ped} \rangle V_{ELM}$, respectively. The conductive part decreases with increasing density, while the convective part appears to remain the same. The amount of the ELM energy that goes to the divertor has been correlated with the total ELM energy released, showing ~ 50% for large ELMs and ~ 80% for small ELMs. The remaining fraction of power is assumed to go to the first

wall. The amount of the power that arrives in the rise phase has been found from simulations[73] to provide the dominant contribution to raising the temperature of the divertor surface. The fraction of power that arrives in the rise phase is found to be about 40% for large ELMs and about 20% for small ELMs. Finally, a factor of 65% is applied to account for the DN plasma imbalance between top and bottom divertors (recall that all ELM energy is assumed to go to the outboard), and this factor is included in ΔW_{ELM}^{div} reported in Table IV. Since the ELM provides a short time scale burst of energy release from the plasma, the inter-ELM heat flux is lower than would be expected if the heat load was completely steady state, and is found to be 9.5 MW/m^2 on the outboard divertor. The temperature increases in Table IV indicate the large ELMs with no footprint expansion will lead to melting, since the tungsten melting temperature is ~ 3400 ^{o}C, while the expanded footprint case may not, depending on the tungsten base temperature determined by overall heat transfer to the coolant. The smaller ELMs appear not to lead to melting for tungsten. For the first wall, tungsten does not appear to reach melting, and neither would ferritic steel (T_{melt} ~ 1500 ^{o}C) or SiC ($T_{decompose}$ ~ 2400 ^{o}C), with operating temperatures of 550-600 ^{o}C and 1000 ^{o}C, respectively.

The divertor has castellated tungsten armor on tungsten structural material and cooling tube. The specific advanced designs are given in refs (60-62), where detailed time dependent modeling is reported. The surface temperature of the armor in these calculations on the plasma side is at ~ 1580^{o}C, while the melting temperature of tungsten is about 3400^{o}C, allowing an 1820^{o}C margin to melting. Detailed analysis[62] indicates that melting will occur unless the average ELM heat flux (ELM energy to divertor divided by the total ELM duration, 6 x $\tau_{||}$) can be kept between 600-800 MW/m^2 when the inter-ELM heat flux is 2 MW/m^2, or between 400-500 MW/m^2 when the inter-ELM heat flux is 10 MW/m^2. These are assuming ELM frequencies in the range of 5-10 Hz, where the ELM frequency is determined from f_{ELM} ~ 0.2-0.4 x $P_{SOL}/\Delta W_{ELM}$.[64] This analysis indicates that the actual surface temperature of the tungsten armor is 1325-1575 ^{o}C under steady state heating of 10 MW/m^2. These lower ELM heat fluxes to reach melting also indicates there is a ratcheting of the inter-ELM temperature upward compared to a single ELM, lowering the allowed heat flux values.

The ELM frequency is derived from a correlation, from tokamak experiments,[65] that gives $f_{ELM}\Delta W_{ELM}$ ~ 0.2-0.4 x P_{SOL}, giving for our power plant example a frequency of about 3.7 /s for large ELMs and 18 /s for small ELMs. These frequencies lead to 1-6x10^8 cycles in a year (which represents a typical time frame for power plants between routine maintenance). Even if melting is avoided, this many cycles may lead to crack growth in the region with the temperature rise. Experiments on the cycling behavior are ongoing, but indicate that cracks may appear even without melting after 10^5 cycles.[74,75] Operating above the DBTT appears to be required to minimize cracking, but only very low energy pulses may be tolerable to obtain little to no cracking. Even if melting is present, but can be tolerated due to benign material movement and very shallow melt layers, it may still accelerate material losses[73].

VII-C. Off-normal heat loading

Off-normal heat loading infers that it occurs infrequently, but has significant magnitude. Plasma disruptions, due to a rapid loss of plasma stored energy and a subsequent loss of plasma current, are the candidates for this loading scenario. Although there is a range of disruption types, major disruptions, which result in the destruction of the plasma configuration, will be addressed. The experimental determination of power fractions to various plasma facing surfaces during disruptions is very imprecise.[76-84] For the ARIES-ACT1 we assume the worst disruption types, the vertical displacement event (VDE) and midplane disruption (MD). For these disruptions the fraction of plasma stored energy that is released in the thermal quench (TQ) is 65-100%. The timescale for the TQ has been correlated with plasma volume, giving a range of Δt_{TQ} = 1.5-2.75 ms. Just like ELMs, the heat load has an asymmetric triangle waveform, rising in about Δt_{TQ}, and falling in ~2-4 of these time scales. This time scale can vary widely even within the same device due to complex dynamics of the thermal quench, which can occur in steps rather than in one drop. JET experiments[81,82] indicate that about 10-50% of the energy released in the thermal quench can go to the divertor, the remainder will be assumed to end up on the first wall. Some small fraction (15%) of energy is observed to be radiated from the plasma during the TQ with a peaking factor of 3.5x, but this will be ignored here. About 25% of the energy released arrives in the rise phase Δt_{TQ}, with the remaining 75% arriving over 2-4 Δt_{TQ}. The deposition area on the divertor target is observed to expand, beyond the steady heat heat load area, during the thermal quench by large factors of 5-10x. Table V shows the parameters used to determine the temperature rise on the divertor and first wall plasma facing surfaces from disruption heat loading.

The plasma stored energy in ARIES-ACT1 is 690 MJ, and in the MD all this energy is released, while in the VDE approximately half of this is released before the thermal quench over a plasma energy confinement time due to wall contact, and the remaining is released in the thermal quench. For disruptions, the heat fluxes are sufficiently large, reaching levels where melting will occur, during the entire TQ duration that the time constant to use in the temperature rise formula is the full $4x\Delta t_{TQ}$ and the 2/3 factor is removed.

Table V. Disruption heat loading parameters for thermo-mechanical analysis.

	MD	VDE
ΔW_{TQ}, MJ	690	345
ΔW_{TQ}^{div}, MJ	69-345	35-173
$A_{TQ}^{div,OB}$, m^2	13.8 (x10)	13.8 (x10)
$\Delta t_{TQ,rise+fall}$, ms	8.0	8.0
ΔT_W, ^oC or ^oK	2250-11260	1125-5630
ΔW_{TQ}^{FW}, MJ	345-621	173-311
$A_{TQ}^{FW,OB}$, m^2	198	198
ΔT_W, ^oC or ^oK	1210-2170	605-1085

$\Delta T_{Fe/SiC}$, ^{o}C or ^{o}K	1660-2980	830-1490

The temperature rises in the divertor are large in spite of footprint expansion, and would lead to melting of tungsten, although the lowest heat load to the divertor in the VDE might avoid this. However, the VDE will release half of the plasma stored energy prior to the thermal quench over about 1-2 seconds, and would likely lead to a bulk temperature increase in both the first wall and divertor structures, making melting likely. For the first wall, although the tungsten temperature rises may be tolerable in the lowest heat load cases, the ferritic steel appears to melt in all cases, and the SiC would likely be compromised. The mitigation of disruptions refers to the injection of particles, whether in the form of pellets, liquids or gases, in order to 1) diminish the conducted/convected heat loads during the TQ, 2) reduce the halo currents and subsequently the electromagnetic forces associated with them, and 3) avoid the generation of runaway electrons. The idea of mitigation is to inject particles before the TQ occurs by detecting some signal of the imminent disruption, although the injection itself induces a TQ. Experiments[76,82-87] show that about 90-100% of the plasma stored energy is radiated with massive gas injection (MGI) of noble gases (Ar, Ne) mixed with deuterium, the technique that has been studied the most. Correspondingly, the heat loads measured in the divertor are only a few percent of the plasma's stored energy. In addition, the plasma current quench time is typically reduced, which must be carefully monitored since this drives stronger EM forces. The halo currents are typically reduced by factors of 2 or larger. Our power plant plasma has a stored energy of 690 MJ, and radiating this to the first wall area, with 80/20 split for the OB/IB, a peaking of 2x assumed, and over the same time scale as a TQ of 4 x Δt_{TQ}, we obtain a temperature rise of 1930 ^{o}C on the outboard and 970 ^{o}C on the inboard for tungsten. We obtain 2650 ^{o}C and 1330 ^{o}C for outboard and inboard, respectively, for Fe and SiC. The values for tungsten may remain under melting, while those for ferritic steel and SiC would appear to lead to melting. For the VDE, it would depend when the mitigation was initiated relative to the wall contact and loss of the plasma stored energy, but may lead to overall lower temperature rises on the first wall, but higher divertor loading. More detailed analysis and experimental demonstrations are necessary to assess credible mitigation scenarios.

If runaway electrons are produced in the current quench, as a result of the strong electric field created by the thermal quench, the first wall damage can be severe due to the local deposition of these particles which have very high energies, as high as ~ 1-20 MeV. Experimental data on runaway electrons deposition is scarce, and difficult to project precisely to future devices. The examination of runaway electrons in JET experiments[83,84] indicates that when runaway electrons are generated, the heat loading changes relative to a current quench without runaways. The magnetic energy in the runaway plasma ranges from 15-50% of the original pre-disruption plasma and the current profile peaks. Using the 50% value, and our li = 0.6 changing to 2.5, we derive a runaway current of ~ 6.2 MA for our power plant. A significant fraction of the magnetic energy can be spent driving eddy currents in the surrounding conductors, and here we assume ~20%. While the plasma current decays from 11 to 6.25 MA, it mainly radiates

the magnetic energy to the first wall similar to a CQ without runaways. The runaway current forms and we assume it occupies all the plasma current, during which there is no longer any radiated power. When the runaway current terminates the magnetic energy in the plasma during the runaway phase either is converted into kinetic energy of runaway electrons (20-60% for JET) impinging on the first wall, or ohmically heats the surrounding plasma, or becomes conducted or convected to the first wall. Finally, a thermal plasma re-emerges after loss of the runaway electrons, which resumes radiating the remaining magnetic energy during the final current quench phase. The deposition area for runaways is a largely unknown parameter, the ITER projections are ~ 0.3-0.6 m^2. Assuming the 30% of the original magnetic energy converted to kinetic energy of runaway electrons, this would give 84 MJ available, and over ~ 1 ms deposition times, would lead to tremendous heat loads. JET experiments[84] indicate the temperature rise of the first wall behaves as ohmic heating, not surface heating like an ELM, and scales with the runaway current squared. Although the runaway electrons will emerge following magnetic field line geometry, their high energy indicates they could penetrate the first wall material to depths approaching the coolant. It is hard to imagine how any runaway electrons would be tolerable in a power plant, without significant first wall armor that would conflict with thermal conversion and tritium breeding.

Activities to establish mitigation of the plasma disruption thermal quench and runaway electron losses are critical to establish the long pulse lengths assumed for tokamak power plants. In addition, the electromagnetic loading on structural materials during the current quench requires analysis to establish the design requirements.

VIII. Regimes that Eliminate or Mitigate Edge Localized Modes (ELMs)

Control of edge localized modes (ELMs) is one of the challenging requirements for the compatibility of a thermonuclear plasma with plasma facing components. The large Type I ELMs occurring in conventional H-mode discharges likely result in unacceptable heat flux to the divertor, which in turn can damage plasma-facing components through either phase changes (e.g. melting) and/or loss of PFC mechanical viability due to repetitive thermal shock (e.g. crack propagation). ELM-free, ELM-suppressed, and small ELM regimes have been found under certain discharge conditions that greatly mitigate the divertor heat load. These options offer significant promise if they can be realized in a reactor scenario, however, these regimes are presently restricted to fairly narrow operational ranges and those regimes that require active methods may be difficult to incorporate in a reactor. Previous publications have reviewed these regimes[88,89] while this section will focus on the presently known restrictions and their implications for achieving these regimes in a reactor configuration.

Experiments indicate that ELMs are triggered by an intermediate toroidal mode number instability, $2 < n < 30$, and are referred to as peeling-ballooning modes.[90-95] These instabilities are driven by steep edge gradients associated with the H-mode pedestal. The steep localized edge pedestal pressure gradient is both the cause and consequence of improved confinement in H-mode since a transport barrier forms near the plasma edge as a result of the steepened gradients. The ELM cycle begins with a buildup in the pedestal

pressure and associated gradients until the gradients trigger the instability, subsequently reducing the pedestal pressure and gradients, and the cycle begins again. The local pedestal pressure gradient drives a bootstrap current density through neoclassical effects and the pressure gradient p' and current density j, contribute to the MHD instability. The instability leads to a rapid flux of heat and particles through the separatrix into the scrape-off layer.

The ELM limits the final edge pressure at a given pedestal width. The EPED-1.6 model[96-98] has been developed to predict both the maximum edge pedestal height and width due to Type I ELM onset by combining constraints due to peeling-ballooning and kinetic ballooning modes. Although not entirely independent, roughly the pedestal steepness is set by MHD stability from low to intermediate n modes, computed using the ELITE code[96], while the pedestal width is set by kinetic ballooning mode onset. These two constraints are generally sufficient to enable unique predictions of the pedestal structure that can be compared to observation. The EPED-1.6 model has successfully been used to predict pedestal parameters in a wide variety of existing and planned experiments[99].

ELM-free regimes offer considerable promise but are presently restricted to somewhat narrow operational ranges. The regimes of most interest are specifically, the Quasi-H (QH) mode, resonant magnetic perturbation (RMP) discharges, the hybrid RMP-assisted QH Mode, Li conditioned discharges, I-mode, and the Enhanced D-alpha (EDA) Mode. Small ELM regimes offer promise for a reactor scenario but are also restricted to narrow operational ranges. The options considered are the Type II and Type III small ELM scenarios, ELM pacing by pellet injection, and the possibility of small ELMs obtained from cross section shaping. These will be described in this section.

Of the possibilities considered, the QH-mode, RMP discharges, and I-mode are all ELM suppression regimes. The Li conditioning option is essentially an ELM free regime and the small ELM regimes should be considered as ELM mitigation techniques. However, especially in the case of RMP discharges, there is a range that varies with devices where the discharges can exist from ELM suppression to mitigation.

VIII-A. Quiescent H-mode and Resonant Magnetic Perturbations

Quiescent H-modes (QH-mode) exhibit H-mode confinement improvement but operate with constant density and radiated power without ELMs. QH-mode operation was first observed in DIII-D counter beam discharges[100] but has now been achieved in other tokamaks, particularly in JT-60U, ASDEX-U, and JET. QH-mode apparently requires a minimum pedestal velocity shear and has now been produced with all co-injection[101] in both DIII-D and JT-60U.

QH-mode is observed over a large range of input neutral beam (NB) power, from 3 MW to 15 MW. The maximum power is limited by a core MHD beta limit. QH-mode is also maintained for long duration (> 4 s or 30 τ_E), limited only by hardware constraints. The pedestal is slightly lower than conventional ELMy H-mode and with a correspondingly

lower performance. QH-mode is almost always associated with the presence of continuous but benign MHD modes known as the Edge Harmonic Oscillation (EHO). As discussed below, the EHO appears to play an important role in keeping the pedestal from reaching the MHD stability limit. The edge particle transport provided by the EHO results in sufficient particle transport to avoid the density buildup associated with ELM-free H-mode operation.

Recent progress has been made in developing a physics basis for the observed ELM suppression in QH-mode discharges. ELITE calculations show that all QH-mode plasmas analyzed to date operate at or near the peeling boundary.[102] This is in contrast to the case when Type I ELMs are present and the discharges usually operate near the conjunction of the peeling and the ballooning section of the stability boundary, and exceed it as part of the ELM cycle. The EHO has, accordingly, been identified as a saturated state of the low-n peeling-ballooning mode.

ELM suppression or mitigation when non-axisymmetric resonant magnetic perturbation (RMP) fields are applied has been observed in many tokamaks[103-108]. First observed in DIII-D, ELM suppression was observed reproducibly with n=3 RMP fields for specific q_{95} values in the ranges 3.4 to 3.7 and 7.0 to 7.2. Type-I ELM mitigation or complete suppression is obtained for a variety of cross section shapes from lower single null (LSN) with both low and high triangularity, δ, to near double null (DN) with high δ, and under conditions with normalized β_N ranging from 1.4 to 2.4, and injected power P_{inj} , ranging between 5 and 15 MW. Reduction or complete ELM suppression has been obtained in plasmas in two distinct density ranges, with collisionality ν^* in the range 0.1 to 0.35 and at high ν^* between 2 and 4. At high ν^*, complete ELM suppression is obtained with an odd parity RMP but with no or limited pedestal density reduction, whereas at low ν^*, suppression is achieved with even parity and is associated with a significant pedestal density reduction. Mitigation was seen with either n = 2 or n = 3 fields but complete suppression has been achieved so far only with n = 3 fields.

Recent experiments in ASDEX-U[105] have reproduced aspects of the ELM suppression by non-axisymmetric external fields observed in DIII-D, though with some significant differences, most notably at much higher collisionality than is typical in the DIII-D experiments. In JET[106] complete suppression has not been observed, but ELM mitigation associated with an increase in ELM frequency and an overall decrease in the ELM energy loss with n=1 and n=2 fields was observed over a large q_{95} range. In the JET experiments, the pedestal density reduction was compensated with gas injection. Evidence of ELM modification in MAST[104] with n=3 and n=2 RMPs has also been found but so far there is no evidence of ELM suppression. Finally in KSTAR, ELMs were suppressed with the application of n=1 magnetic perturbations[109], and with the application of lower hybrid waves in EAST[110]. Several major experiments, ASDEX-U, NSTX, DIII-D, JET, and MAST, are planning coil upgrades to investigate further the physics of 3D field effects. ITER is considering a decision on whether to install a similar coil system.

RMP discharges generally have slightly lower performance and pedestal height than conventional ELMy H-mode. The physics responsible for the effects on ELMs is

unknown but some progress has been made in understanding some of the features of ELM suppression. One key aspect is that unlike in conventional H-mode, heat transport and particle transport are somewhat decoupled. Essentially, particle transport is increased but energy transport remains only slightly reduced from H-mode levels. RMP ELM suppressed discharges are generally found to be stable to peeling-ballooning modes.[96,103,104] Analysis with the EPED1 model suggests that the RMP suppresses ELMs by constraining the expansion of the pedestal width, which, combined with a pressure gradient limit due to the KBM, results in peeling-ballooning modes remaining stable, preventing ELM onset.[111]

Non resonant magnetic fields (NRMFs) from the I- and C-coils in DIII-D provide an additional knob to change the pedestal velocity shear and allow sustained operation with a QH-mode edge and zero-net NBI rotational torque.[112] In DIII-D, the counter NBI torque required for QH-mode decreases with increasing β_N and an increasing NRMF from the addition of an n=3 field from the C-coils. The torque from the NRMF replaces the NBI torque and opens a new path to QH-mode with little or no NBI torque. NRMFs are easy to apply and can utilize external coils. There is also no adverse impact of the NRMF on the energy confinement and resilience to locked modes is actually improved. This allows operation with low rotation and low density at high β without either tearing modes or locked modes.

VIII-B. Lithium conditioning

ELM-free operation was observed in NSTX[113] after application of lithium to condition the walls of the device. Depending on the level of Li conditioning, the possibilities range from ELMy to infrequent ELMs to ELM-free discharges. Full ELM-free operation, however, apparently requires a relatively high lithium deposition threshold, although the plasma parameters improve nearly continuously with pre-discharge lithium evaporation.[114] The physics responsible for the ELM suppression is not completely known but it is thought that the change in the density profile from Li via recycling reduction from Li, coupled with an invariant edge temperature profile due to ETG modes, is an important item. The main obstacle to the NSTX Li conditioning scenario is the impurity accumulation that accompanies the ELM-free H-mode since ELMs actually flush impurities and prevent this accumulation.

In contrast to DIII-D and other experiments, in NSTX it appears that ELMs are actually initiated in the ELM-free Li conditioned plasmas by adding a small non-axisymmetric field perturbation.[115] The triggering of ELMs in conjunction with the Li conditioning could then provide an additional tool to regulate the ELMs and thereby control both the impurity accumulation and the impact of ELMs on the divertor.

VIII-C. I-Mode and Enhanced D-Alpha regime

I-Mode, first observed in C-Mod[116,117], is characterized by operation without ELMs, while having H-mode energy confinement and L-mode particle confinement with no steep density pedestal. Thus, there is no particle barrier and consequently no impurity

accumulation. Obtained primarily in configurations with "unfavorable" ∇B drift for H-mode access (i.e. with ion grad-V drift pointed away from the primary X-point)[118], the I-mode yields an H-mode factor $H_{98} \sim 1$ at $\nu_e^* \sim 0.1$. Associated with I-mode is a continuous, weakly coherent 100-200 kHz fluctuation seen in the edge density, temperatures, and magnetic field that appears to be related directly to increased particle transport. The I-mode has now been reliably reproduced in ASDEX-U[119] and recent experiments in DIII-D appear to have reproduced discharges with similar features to an I-mode before H-mode transitions, but with a weaker confinement factor. Recent analysis of an example I-mode pedestal in C-Mod shows that it exists far from the peeling-ballooning stability boundary[120], consistent with the observed lack of ELMs.

The I-mode scenario also offers operation at low collisionality. Recent analysis[121], using simple scaling assumptions combined with modeling and experimental data, suggests that I-mode can be scaled to ITER and to a reactor, as the power thresholds for the L-mode to I-mode and the I-mode to H-mode transitions allow a feasible path to high gain. The density scaling is also favorable. In addition, C-Mod data shows that confinement degradation in I-mode is very weak, as the stored energy increases almost linearly with the heating power.

The Enhanced D-Alpha (EDA) is characterized by operation without ELMs while maintaining relatively high pedestal gradients in ICRF heated discharges[122]. The EDA, however, has only been observed reliably so far in C-Mod, although a similar mode has been observed in JET. The key to obtaining this state is apparently increased recycling. While the D-Alpha light signal actually increases, confinement improves and high pedestal gradients are subsequently obtained. This is in contrast to conventional H-mode where the improved confinement is associated with a sharp decrease in the D-Alpha signal. The EDA regime is associated with the quasi-coherent mode (QCM), located in the pedestal with a high frequency, which regulates particle transport. In addition to the requirements for ICRF heating and high recycling at the edge, the major restriction to the EDA is that it appears to have limited operational range. EDA operation in C-Mod is most easily accessed in intermediate δ and q_{95} in the ranges $0.3 < \delta < 0.55$ and $q_{95} > 3.5$.

VIII-D. Small ELM regimes

Type II ELMs[123,124] and similar options, the so-called "grassy ELMs and Type V ELMs[125] show promise since they are more frequent but reduced size compared to Type I ELMs. These have been observed in JT-60 and JET, and occasionally in DIII-D[126] and ASDEX-U[127]. In JT-60U[125], the ELM frequency increases from about 50 kHz for Type I ELMs to 533 kHz in the Type II regime, with a corresponding reduction in the power incident on the divertor from the much reduced ELM size from 21 MW/m^2 to 1.7MW/m^2.

The required conditions for obtaining this scenario are high elongation and triangularity, $\kappa > 1.8$, and $\delta > 0.5$, low collisionality, $\nu^* < 1$, low current, and small rotation – either co-rotation or counter-rotation. With finite co-rotation (~1 kHz) higher β_p seems to be required. The direction of the toroidal rotation seems to be more important than the rotation shear. While the overall heat load at the divertor is greatly reduced in Type II

ELMing discharges, the major drawback is that, in addition to the restricted operational range, it is not reliably reproducible, with most of the known cases from JT-60U. In addition, there is an overall reduction in plasma performance from Type I H-mode levels so that the pedestal is usually lower than conventional ELMing H-mode.

Type III ELMing discharges also offer the promise of small ELM operation with limited impact on the divertor[125]. Type III regimes with small ELMs tend to appear for defined regions of δ, q_{95} and proximity to double null. So far, this regime occurs only at low electron temperature near the H-mode threshold, with the critical temperature scaling inversely with the electron density. This is generally associated with reduced confinement. Nevertheless, the pedestal pressure can be near Type I ELM H-mode values since $T_e \sim 1/n_e$. This is thought to be due to resistive instability in contrast to the Type I ELM precursor.

While offering promise, the Type III option has several drawbacks. First, the Type III ELM regime is also not reliably reproducible and has not been observed in all tokamaks. Further, the ELM frequency decreases with increased heating, which is unfavorable. The Type III regime transitions to a conventional Type I ELM regime when the heating power is sufficiently above the L to H-mode transition.

VIII-E. ELM Pacing

It has been observed for some time that injection of frozen hydrogenic pellets into an H-mode discharge can trigger ELMs.[127] If the pellets are injected sufficiently rapidly, each one triggers an ELM and the result is smaller and more frequent ELMs. Recent promising results have now been obtained on controlling ELMs by pellet pacing with small pellets.[128] This scenario requires only the hardware for injecting pellets. However, considerable further research is required to fully understand the mechanism for triggering ELMs and to optimize the size, speed, and position and angle of injection. One issue that will need to be addressed in optimizing pellet pacing is balancing the needs of using pellets for fuelling deep into the core from the high field side, and for ELM control, which requires small pellets launched from the low field side, that penetrate essentially only the edge region. Optimization in present machines should provide an acceptable scenario. Additional data from ITER should yield crucial information on the prospects of pellet pacing in burning plasmas.

VIII-F. Strong outboard squareness

Modification of the shape of the outer boundary changes the unstable spectrum by changing the field line length in the outer bad curvature region. In particular, higher squareness makes the higher n modes relatively more unstable.[129] According to the present understanding of ELMs, this should result in smaller but more frequent ELMs. This has been verified in several experiments in DIII-D[130], which found an optimum squareness for small ELMs. Given sufficient flexibility in the shape control, this effect can be achieved in a wide variety of conditions since it depends most essentially on the cross section shape. However, while this technique allows additional control of ELMs,

there is a significant performance loss as the pedestal pressure is reduced as the ELMs become smaller.

VIII-G. Discussion

The features of the ARIES-ACT1 plasma should be examined when considering viable ELM suppression or mitigation approaches, although extrapolation to the reactor regime is difficult. The plasma is both at high density and high temperature, a difficult combination to reproduce on present tokamaks. The pedestal temperature is ~ 4 keV while the density is ~ 0.9-1.0x10^{20} /m^3, yielding a pedestal collisionality of ~ 0.1. Plasma shaping is strong with an elongation of 2.2 and triangularity of 0.63 at the separatrix, and the configuration is up-down symmetric double null. The edge safety factor is high at $q_{95} \geq 4.5$ as a result of minimizing the plasma current and required external current drive. The combination of the alpha power and auxiliary power is 2.5-3 times the L to H threshold power in the flattop phase, and the core plasma radiated power is about 25% of this input power. The density is at the Greenwald density, and although it is not a fundamental limit, may influence the pedestal and ELM regime depending on the resulting SOL density. The highly radiating divertor requires high density there, and this would relate back to separatrix and pedestal parameters. Some of these parameters would favor small ELM magnitudes and/or convective rather than conductive ELM transport. However, the associated high temperatures make the collisionality as low as expected on ITER. Relying on regimes that exist near the L-H threshold appear to be out of the question with such a large power standoff. The use of external systems to provide 3D magnetic fields will be limited by the proximity of those coils to the plasma, since they must be placed behind the blanket and shield, along with the resistive wall mode and vertical position feedback coils, to reduce the neutron damage. It is not known how the various ELM regimes scale to $\beta_N > 5$, and ARIES-ACT1 has high internal safety factor q with a flat, low shear profile. It is not yet clear how this affects the coupling of the edge pedestal stability to core. Earlier studies suggest that this may make the peeling-ballooning modes more global, leading to larger ELMs.[131] In addition the role of a nearby conducting wall in the wall-stabilized regime ARIES-ACT 1 is not known, although, stabilization of intermediate n modes typically requires a closer wall than is the case in most tokamaks. Addressing ELM mitigation on ITER is a high priority and is being pursued vigorously on experimental tokamaks[132], however, extension to the power plant regime is likely to further constrain the successful techniques.

IX. Tritium burnup, fueling and exhaust

The amount of the injected tritium (and deuterium) that is actually consumed in fusion reactions within the plasma, before it leaves the plasma chamber is an important parameter for fueling, exhaust, and the tritium inventory in the associated processing circuit. This is usually characterized by a parameter called the tritium burnup fraction, defined as the ratio of the tritium consumed to tritium supplied in steady state, and often has values ranging from a few to 10's of percent. This is given by

$$f_b = \frac{n_D n_T \langle \sigma v \rangle_{DT}}{n_D n_T \langle \sigma v \rangle_{DT} - \frac{n_T}{\tau_T^*}} = \frac{1}{1 + \frac{1}{n_D \tau_T^* \langle \sigma v \rangle_{DT}}}$$

Where n_D and n_T are the deuterium and tritium fuel ion densities, τ_T^* is the total tritium residence time in the core plasma, and $\langle \sigma v \rangle_{DT}$ is the DT velocity averaged reactivity. The critical parameter that gives rise to uncertainty in this expression is the residence time. All other quantities are known, and can be treated rigorously. The expression here is a global approximation and would actually be defined as an integral over the plasma volume, and for approximate calculations one would use volume averaged quantities in this expression. The value of this number has a strong impact on the amount of tritium needed in the fueling/exhaust loop, and the throughput itself. For example, with a burnup fraction of 10 % and 2500 MW of fusion power, which consumes 139 kg of tritium per year, one is injecting 1390 kg and extracting 1250 kg of tritium each year. Based on present fueling experiments[133-135], power plant plasmas will be fueled by pellet injection from the high field side, in order to access the deepest penetration of the fuel to the plasma core where the highest fusion reaction rates exist. This fuel will subsequently be consumed or will transport out of the plasma without being consumed. Once the plasma particles cross the plasma separatrix they enter the scrape-off layer, where they can be transported to the divertor or to the first wall. At solid surfaces the ions and electrons are recombined, and desorb as neutral atoms or molecules, with energies corresponding to the wall temperature. If these particles impinge on the solid surfaces with elevated energy they can induce sputtering of the wall material, and/or implant themselves deeper into the material surface. In addition, some particles which enter the divertor can be pumped out of the plasma chamber. Neutral particles can transport themselves back across the SOL, from the first wall or divertor, to the main plasma and re-enter it. This is in fact how virtually all tokamak experiments are fueled, predominantly from the edge, although neutral beams also contribute to central fueling on present experiments. The neutral particles will penetrate the plasma until they are ionized and become part of the plasma population, at which point they will respond to plasma transport. On existing tokamaks, this process can easily bring particles to the plasma core. On future tokamaks[136], it is anticipated that this process will become significantly less efficient due to higher electron temperature and density at the plasma edge ($T_{ped} \sim 5$ keV and $n_{ped} \sim 1 \times 10^{20}$ /m^3 in ITER for example). The average neutral penetration distance into the plasma is then strongly reduced. This distance can be defined as[137]

$$\Delta_{neut} = 2\, V_{thn} / (\sigma_i\, V_{the}\, E\, n_{e,ped})$$

where V_{thn} is the average neutral particle velocity, σ_i is the ionization cross-section, V_{the} is the electron thermal velocity, $n_{e,ped}$ is the electron pedestal density, and E is a factor to account for poloidal variations in fueling efficiency. Missing from this expression is the effective diffusion of neutrals generated by multiple charge exchange events. In addition, a large SOL width will contribute to weaker fueling efficiency if the neutrals have a high probability of being ionized in the SOL. From a model used in ref (138) originally for He, an expression can be written for the mean time a triton spends in the

core plasma accounting for its introduction via pellet injection into the core and its multiple re-introduction via recycling and penetration,

$$\tau_T^* = \tau_{T,1} + (R_{eff}/(1-R_{eff}))\ \tau_{T,2}$$

where $(R_{eff}/(1-R_{eff}))$ is the mean number of times a triton is returned to the core plasma before being pumped out, R_{eff} is the ratio of tritons entering the plasma to tritons leaving the plasma (and $1-R_{eff}$ is an exhaust efficiency), $\tau_{T,1}$ is the core particle confinement time (typically ~ τ_E), and $\tau_{T,2}$ (expected to be < τ_E) is the average time spent inside the core plasma after being recycled from walls or divertor and re-entering the core plasma. This is derived from a two population model for helium, where the first population is the "birth" population, and the second is the recycled population. The same model can be used for tritium or deuterium, since the birth is the pellet injection deposition, and the recycled fuel is the second population. The particle confinement times in the plasma core for deuterium, tritium, and helium are expected to be similar, since they are all light ions with low Z, although this has not been experimentally demonstrated in a burning plasma. More precise assessments for the core τ_p and τ_p^* can be obtained in UEDGE simulations.[10] The presence of He and its particle confinement introduces the other aspect that must be included when discussing fuel burnup fraction when $\tau_T^* \sim \tau_D^* \sim \tau_{He}^*$, which is fuel dilution in the core plasma. Large values of the overall particle confinement time, τ_p^*, would lead to high fuel burnup fractions which would reduce the amount of tritium that was cycled through exhaust and fueling, but would also lead to high core helium content and fuel dilution, reducing the fusion power output. Therefore, studying fuel burnup without accounting for the self-consistent impact on the core plasma power balance is not appropriate. Ideally it is desired to make the hydrogen species have a large particle confinement time, and the helium a very short confinement time.

The systems analysis used in these studies to identify operating points automatically solves for the self-consistent power balance and helium content, including impurities and various radiation sources, given an input τ_p^*/τ_E. The operating point scans for ARIES-ACT1 assumed a value of $\tau_p^*/\tau_E = 5$, a typical value achieved on pumped divertor tokamak experiments[136-140] and also used in ITER analysis. Shown in Figure 19 are the operating spaces for various values of τ_p^*/τ_E assuming the ARIES-ACT1 plasma geometry, toroidal field, q_{95}, impurity fraction, current drive efficiency, and β_N, while scanning τ_p^*/τ_E from 1 to 15, density profiles with n(0)/<n> from 1.27 to 1.42, temperature profiles T(0)/<T> from 2.1 to 3.0, fusion gain Q from 15 to 50, and n/n_{Gr} from 0.8 to 1.2. The viable operating points lie inside the contours. These scans are necessary to find solutions as τ_p^*/τ_E changes due to its impact on power and particle balance. The operating spaces would be broader if all parameters had been scanned, but it is of interest to see how a parameter as uncertain as τ_p^*/τ_E affects a given design. In addition, an electric power constraint is imposed on the resulting database generated by the systems code, first a wide range from 500 to 1500 MW, and then a narrower range appropriate to ARIES designs at ~ 1000 MW. The power constraint is critical since variations in plasma profiles and central temperature and density values could yield many solutions of no interest at very low or very high fusion powers. Constraints on the normalized beta, global energy confinement, and peak divertor heat flux, the same ones

imposed for the ARIES-ACT1 design, are used to filter solutions. With the wide electric power range values from $\tau_p^*/\tau_E = 2 - 11$ can be accommodated, resulting in fusion powers from 1300 to 2400, core helium fractions from 3-19%, and tritium burnup fractions from 5-24%. Restricting the electric power to ~ 1000 MW, $\tau_p^*/\tau_E = 2 - 7$ can be accommodated, with helium fractions of 3-15%, and tritium burnup fractions of 6-14%. Finally, if the density is restricted to be less than or equal to the Greenwald density, as in ARIES-ACT1, the allowable ranges shrinks further, with $\tau_p^*/\tau_E = 2 - 5$, the upper limit coinciding with the original assumption. The reference point is shown, which is determined to have a tritium burnup fraction of 13.7%.

Another approach to determine the tritium burnup fraction is to use the helium exhaust requirement and scaling of the DT exhaust rate to core plasma and divertor neutral density ratios. For the ARIES-ACT1 design, the fusion power is 1815 MW, which translates into 6.45×10^{20} reactions/s, where a deuteron and a triton are consumed, and a helium nuclei is produced. In steady state the helium density fraction (relative to the electron density) is 0.097, and the DT fuel is 0.752, the remainder being 0.003 of argon. In steady state the helium exhaust rate must match the helium production rate, which is 6.45×10^{20} /s or 7.7 Pa-m^3/s (assuming a $T_{wall} = 873^oK$). Here we will ignore the small levels of He or DT particle losses into solid materials. The corresponding rate of DT exhaust can be established with the ratio of the core density fractions, $E_{DT} = (f_{DT}/f_{He})\, E_{He}$. However, the actual exhaust rate would depend on the distribution of helium and DT fuel at the pump mouth. It is observed that the fuel to helium ratio can be different in the core plasma and the divertor, and this difference is characterized by the helium enrichment factor, $\eta_{He} = (n_{He}^o/2n_{DT}^o)/(n_{He}/n_e)$, where the superscript "o" refers to neutrals (n_{DT} refers to any molecular form of D or T) . This parameter varies widely[139-143], but is typically assumed to be less than 1.0.[136] Including this the exhaust rate for DT is $E_{DT} = (1-2f_{He}\eta_{He})/(f_{He}\eta_{He})\, E_{He}$. The fueling rate ($F_{DT}$) is the same as the exhaust rate with the addition of the consumed fuel, $2E_{He}$. For $\eta_{He} = 0.2$, $E_{DT} = 3.2 \times 10^{22}$ particles/s or 383 Pa-m^3/s of DT atoms, or 192 Pa-m^3/s of DT molecules. The fueling is then 399 Pa-m^3/s DT atoms. Based on this analysis the tritium burnup fraction ($2E_{He}/F_{DT}$) would be 3.9%, while if $\eta_{He} = 1.0$, the tritium burnup fraction would reach 19%. The corresponding He enrichment for the 13.7% burnup, estimated using core plasma parameters, is 0.75.

The self-consistent determination of fueling, core plasma transport, recycling, plasma-material interactions, and exhaust, in conjunction with a divertor plasma-neutral solution is challenging due to the strong interconnections of these physics phenomena. 1.5D simulations[144,145] using correlations based on 2D edge plasma and kinetic neutrals[51,146] have been done for ITER in order to identify operating windows. The particle behavior will be critical to controlled operation of any burning plasma and significantly more activity is required in present tokamak experiments to establish the physics basis.

X. Conclusions

The ARIES-ACT1 study has examined an advanced physics and advanced technology tokamak power plant configuration. The physics regime is characterized by high β_N^{total} (above the no wall limit, ~ 5.75) and high global energy confinement (H_{98} ~ 1.5-1.6).

Ideal MHD analysis of low-n kink and high-n modes indicate that the broad pressure plasmas are stable with a conducting shell on the outboard and some combination of plasma rotation, feedback control, and/or kinetic stabilization. Vertical stabilization is achieved by conducting shells on the outboard and inboard, along with feedback coils located behind the blanket and shield. New developments in describing the power scrape-off width have resulted in higher peak heat fluxes in the divertor than those determined during the ARIES-AT study. The plasma major radius has increased from 5.5 to 6.25 m primarily to accommodate this by providing larger area for power deposition. Developments in describing the maximum pressure at the pedestal, using peeling-ballooning theory, allow this transport feature to be consistently included in the plasma density and temperature profiles, with $n_{ped} \sim 0.9\text{-}1.0 \times 10^{20}$ /m^3 and $T_{ped} \sim 4.0$ keV. Time dependent free-boundary transport simulations with TSC and TRANSP are used for the first time in power plant studies to provide the self-consistent plasma rampup and relaxed flattop configurations, with current and energy transport, heating and current drive, bootstrap current, and fast particle assessments. Accurate determination of the volt-seconds required to bring the plasma to full current with heating and current drive assist, ~ 160 V-s, are established. With 40 MW of lower hybrid and 20 MW of ion cyclotron heating and current drive as the reference sources, 20 MW of additional electron cyclotron was also examined for its deposition flexibility for modifying the q-profile. Due to the difficulty in describing energy transport in advanced tokamak regimes, a range of temperature and density profiles were examined, showing that the broad pressure cases ($p_o/\langle p \rangle \sim 2.3\text{-}2.4$) could reach the desired fusion performance, while remaining ideal MHD stable, and more peaked pressure could be tolerated with an increase in the toroidal field and a reduction in β_N^{total}. The fast particle MHD stability is addressed for the first time, indicating that instabilities lead to redistribution to larger minor radii and not losses, although the plasma configurations identified here are expected to be sensitive to small changes in $T_i(0)$, $q(0)$, and β_{fast}. Simulations of the scrape-off layer plasma and divertor are done for the first time in the ARIES studies to explore the detached highly radiating divertor regime, and point to divertor geometry and feedback control as possible approaches to the high radiated powers needed in power plants.[10] Examination of the heat loading for transient (ELMs) and off-normal (disruption) with simple formulations based on experimental observations was done, indicating the strong limitations when going to the power plant regime. ELMs will require a reduction in their magnitude, however, the large number of cycles experienced in a power plant will make cracking a severe issue that could limit the magnitude further. The wide range of ELM observations in experiments for eliminating ELMs or mitigating them is encouraging, however extrapolation of these results to the power plant plasma regime is very difficult at present. Although disruption mitigation may distribute the thermal quench energy more effectively, tolerating runaway electrons appears nearly impossible. Continued experimental studies on avoiding and mitigating all disruption phases is critical for tokamak power plants. The behavior of fusion fuel, helium ash, and impurity particles in the tokamak presents a complex and interconnected problem that is particularly difficult to analyze in detail. The tritium burnup fraction continues to be a challenging parameter to determine precisely, since it requires precise knowledge of several parameters, although continued integration of 2D SOL plasma, neutrals, and core plasma analyses can define the range more accurately. Experimental benchmarking of

particle aspects will be necessary to develop confidence in sustaining and controlling a burning plasma.

Acknowledgements

Work supported by DOE contracts DE-AC02-76CH03073, DE-AC52-07NA27344, and DE-FC02-04ER54698.

References

1. C. E. KESSEL et al, *Fusion Eng. Design,* **80**, 63, (2006).
2. S. C. JARDIN et al, *Fusion Eng. Design*, **80**, 25, (2006).
3. S. C. JARDIN et al, *Fusion Eng. Design*, **38**, 27, (1997).
4. Z. DRAGOJLOVIC et al, *Fusion Eng. and Design,* **85,** 243, (2010).
5. S. C. JARDIN et al, *J. Comput. Physics*, **66**, 481, (1986).
6. M. S. TILLACK et al, this issue
7. W. M. TANG, *Nucl. Fusion*, **26**, 1605, (1986).
8. C. E. KESSEL et al, *Nucl. Fusion*, **47**, 1274, (2007).
9. P. SNYDER et al, *Plasma Phys. Controlled Fusion*, **46**, A131, (2004).
10. T. D. ROGNLIEN and M. E. RENSINK, this issue.
11. Y. MARTIN et al, *J. Physics Conf. Series*, **23**, 012033, (2008).
12. R. C. GRIMM et al, *J. Comp. Physics,* **49,** 94, (1983).
13. J. M. GREENE et al, *Nucl. Fusion*, **21**, 453, (1981).
14. J. DELUCIA et al, *J. Comp. Physics*, **37**, 183, (1980).
15. A. BONDESON and D. J. WARD, *Phys Rev Lett*, **72,** 2709, (1994).
16. D. J. WARD and A. BONDESON, *Phys Plasmas*, **2,** 1570, (1995).
17. A. M. GAROFALO et al, *Nucl Fusion*, **47,** 1121, (2007).
18. Y. Q. LIU et al, *Phys Plasmas*, **7,** 3681, (2000).
19. L. J. ZHENG, M. T. KOTSCHENREUTHER, and J. W. VAN DAM, *Nucl Fusion*, **49,** 075021, (2009).
20. K. GHANTOUS et al, *Phys. Plasmas*, **19,** (2012).
21. N. N. GORELENKOV, H. L. BERK and R. V. BUDNY, *Nucl. Fusion*, **45**, 226, (2005).
22. C. Z. CHENG, *Phys. Reports*, **211**, 1 (1992).
23. W. W. HEIDBRINK et. al. *Nucl. Fusion*, **48**, 084001 (2008).
24. M. A. VAN ZEELAND et. al. *Phys. Plasmas*, **18**, 056114 (2011).
25. W.W. HEIDBRINK et.al., *Nucl. Fusion,* (2013) submitted.
26. M. GREENWALD et al, *Nucl Fusion,* **28**, 2199, (1988).
27. ITER Physics Basis, Transport and Confinement, *Nucl Fusion*, **39**, 2175, (1999).
28. J. ONGENA et al, *Phys Plasmas*, **8**, 2188, (2001).
29. M. A. MAHDAVI et al, *Nucl Fusion*, **42**, 52, (2002).
30. V. V. ALIKAEV et al, *Plasma Phys Reports*, **26**, 991, (2000).
31. G. MANK et al, *Phys Rev Lett*, **85**, 2312, (2000).
32. G. SAIBENE et al, *Plasma Phys Control Fusion*, **44**, 1769, (2002).
33. D. W. IGNAT et al, *Nucl. Fusion*, **34**, 837, (1994).
34. P. BIBET et al, *Nucl Fusion*, **35**, 1213, (1995).

35. A. BECOULET et al, *Fusion Engr and Design*, **86**, 490, (2011).
36. R. W. HARVEY AND M. G. MCCOY, 1993 Proc. Of the IAEA Technical Committee on Advances in Simulation and Modeling of Thermonuclear Plasmas (Montreal, Quebec) (Vienna: IAEA) pg 489. USDOC NTIS Doc. No. DE93002962.
37. A. SMIRNOV et al, in Proceedings of the 15th Workshop on ECE and ECRH, World Scientific, 2009, p. 301.
38. P. T. BONOLI et al, Proc. 21st International Conference on Fusion Energy (Chengdu, 2006) (Vienna:IAEA) CD-ROM file PD-3 and http://www-naweb.iaea.org/napc/physics/FEC/FEC2006/html/index.html.
39. J. H. BELO et al, *Nucl. Fusion*, **51**, 083017, (2011).
40. M. BRAMBILLA, "A full wave code for ion cyclotron waves in toroidal plasmas", Report IPP 5/66, Max Planck Institute for Plasma Physics.
41. R. J. GOLDSTON et al, *J Comput Physics*, **43**, 61, (1981).
42. D. W. SWAIN AND R. H. GOULDING, *Fusion Engr Design*, **82**, 503, (2007).
43. T. K. MAU, Proc. 17th IEEE Symposium on Fusion Engineering, 1997, (Institute for Electrical and Electronics Engineers, Piscataway, New Jersey, 1997).
44. M. A. HENDERSON et al, *Nucl Fusion*, **48**, 054013, (2008).
45. N. B. MARUSHCHENKO et al, *Phys. Plasmas*, **18**, 032501, (2011).
46. A. H. KRITZ et al, Heating in Toroidal Plasmas, *Proc. 3rd Joint Varenna-Grenoble Int. Symp (Grenoble, 1982), vol 2 (Brussels, CEC), pg 707, 1982.*
47. Y. R. LIN-LIU et al, *Phys. Plasmas*, **10**, 4064, (2003).
48. K. TAKAHASHI et al Fusion Sci Tech **47** 1 (2005).
49. T.D. ROGNLIEN and M.E. RENSINK, Fusion Eng. Design, **60**, 497, (2002).
50. S.I. BRAGINSKII, "Transport Processes in a Plasma," Reviews of Plasma Phys., edited M.A. Leontovich (Consultants Bureau, New Youk, 1965), Vol. I, p. 205.
51. A.S. KUKUSHKIN et al., *Nucl. Fusion*, **43**, 716, (2003).
52. A.S. KUKUSHKIN et al., "Consequences of a reduction of the upstream power SOL width in ITER," J. Nucl. Maters. (2013), in press, jttp://dx_doi.org/10.1016/j.nucmat.2013.01.027.
53. D.E. POST, *J. Nucl. Mat*, **220-222**, 143, (1995).
54. C. E. KESSEL et al, *Fus Sci & Tech*, accepted for publication.
55. W. FUNDAMENSKI et al, *Nucl. Fusion,* **45,** 950, (2005).
56. W. FUNDAMENSKI et al, *Nucl. Fusion,* **51,** 083028, (2011).
57. T. EICH et al, *Phys. Rev. Lett.,* **107**, 215001, (2011).
58. R. GOLDSTON, *Nucl. Fusion,* **52,** 013009 (2012).
59. R. A. PITTS et al, *J. Nucl. Mater.,* **415,** S957 (2011).
60. M. S. TILLACK et al, *Fusion Engr Design* **86**, 71, (2011).
61. Y. MINAMI, et al, this issue.
62. J. P. BLANCHARD et al., this issue.
63. H. URANO et al, *Plas Phys Control Fus,* **45,** 1571, (2003).
64. A. LOARTE et al, *Plas Phys Control Fus,* **45,** 1549, (2003).
65. A. HERMANN et al, *J Nuc Mat,* **313-316,** 759, (2003).
66. G. F. MATTHEWS et al, *Nuc Fus,* **43,** 999, (2003).
67. A. LOARTE et al, *Phys Plas,* **11,** 2668, (2004).
68. T. EICH et al, *J Nuc Mat,* **337-339,** 669, (2005).
69. A. LOARTE et al, *Phys Scr,* **T128,** 222, (2007).

70. T. EICH et al, *J Nuc Mat,* **415,** S856, (2011).
71. H. THOMSEN et al, *Nuc Fus,* **51,** 123001, (2011).
72. M. SUGIHARA et al, *Plasma Phys. Controlled Fusion,* **45,** L55, (2003).
73. G. FEDERICI et al, *Plasma Phys. Controlled Fusion,* **45,** 1523, (2003).
74. I. E. GARKUSHA et al, *Phys. Scr.,* **T138,** 014054, (2009).
75. TH. LOEWENHOFF et al, *Phys. Scr.,* **T145,** 014057**,** (2011).
76. V. RICCARDO et al, *Nuc Fus,* **45,** 1427, (2005).
77. J. I. PALEY et al, *J Nuc Mat,* **337-339,** 702, (2005).
78. P. ANDREW et al, "Heat Load to the JET Divertor During Disruptions and Disruption Mitigation by Massive Gas Puffing", *30st EPS Conf on Contr Fus and Plasma Phys*, St. Petersburg, July 7-11 2003, vol 27A, P-1.108, ECA.
79. G. PAUTASSO et al, "Details of Power Deposition in the Thermal Quench of ASDEX Upgrade Disruptions", *31st EPS Conf on Contr Fus and Plasma Phys*, London, June 28-July 2 2004, vol 28G, P-4.132, ECA.
80. E. M. HOLLMANN et al, "Observation of Main-Chamber Heat Loads During Disruptions in DIII-D", *31st EPS Conf on Contr Fus and Plasma Phys*, London, June 28-July 2 2004, vol 28G, P-2.182, ECA.
81. A. LOARTE et al, "Expected Energy Fluxes onto ITER Plasma Facing Components During Disruption Thermal Quenches from Multi-Machine Data Comparisons", *Proc 20th IAEA Conf Fusion Energy*, Portugal, Nov 1-6 2004, http://www-naweb.IAEA.org/napc/physics/fec.htm.
82. G. ARNOUX et al, *J Nuc Mat,* **415,** S817, (2011).
83. A. LOARTE et al, *Nuc Fus,* **51,** 073004, (2011).
84. M. LEHNEN et al, *Nuc Fus,* **51,** 123010, (2011).
85. M. SUGIHARA et al, *Nuc Fus,* **47,** 337, (2007).
86. R. S. GRANETZ et al., *Nuc Fus* , **46,** 1001, (2006).
87. D. G. WHYTE et al., *J Nuc Mat,* **363-365,** 1160, (2007).
88. N. OYAMA et al., *Plasma Phys Control Fusion*, **48**, A171, (2006).
89. K. KAMIYA et al., *Plasma Phys Control Fusion*, **49**, S43, (2007).
90. E.J. STRAIT et al., in Proc. 20th Europ. Conf. on Controlled Fusion and Plasma Physics (Lisbon 1993) (Vol. 17C (part I) (Geneva: EPS) p211 (1993).
91. J.W. CONNOR et al., *Phys. Plasmas*, **5**, 2687, (1998).
92. T.H. OSBORNE et al., *J. Nucl. Mater*, **266-269**, 131, (1999).
93. H.R. WILSON et al., *Phys. Plasmas*, **6,** 1925, (1999).
94. P. B. SNYDER et al., Phys Plasmas, **9**, 2037, (2002).
95. S. SAARELMA et al., *Plasma Phys. Control. Fusion*, **51**, 035001, (2009).
96. P. B. SNYDER et al., *Nucl. Fusion*, **49**, 085035, (2009)
97. P. B. SNYDER et al., *Phys. Plasmas,* **16**, 056118, (2009).
98. P. B. SNYDER, et al., *Nucl. Fusion*, **51**, 103016, (2011).
99. J.R. WALK et al., *Nucl. Fusion*, **52**, 063011, (2012).
100. K.H. BURRELL et al., *Phys. Plasmas*, 12, 056121, (2005).
101. K.H. BURRELL, et al., *Phys. Rev. Lett*., 102, 155003, (2009).
102. P.B. SNYDER et al., *Nucl. Fusion*, **47**, 961, (2007).
103. T. E. EVANS et al., *Nat. Phys*., **2**, 419, (2006).
104. M. FENSTERMACHER et al., *Phys. Plasmas*, **15**, 056122, (2008).
105. W. SUTTROP et al., *Fusion Eng. Design*, **84**, 290 (2009).

106. Y. LIANG, et al., *Phys. Rev. Lett*, **98**, 265004, (2007).
107. A. KIRK et al., *Nucl Fusion*, **50**, 034008, (2010).
108. C. SONTAG et al., *Nucl. Fusion*, **47**, 1005, (2007).
109. Y. M. JEON, *Phys. Rev. Lett*., **109**, 035004, (2012).
110. Y. LIANG, *Phys. Rev. Lett*., **110**, 235002, (2013).
111. P. B. SNYDER et al., *Phys. Plasmas*, **19**, 056115, (2012).
112. A. M. GAROFALO et al., *Nucl. Fusion*, **51**, 083018, (2011).
113. R. MAINGI et al., *Phys. Rev. Lett*, **103**, 075001, (2009).
114. R. MAINGI, *Phys. Rev. Lett*, **107**, 145004, (2011).
115. J. M. CANIK, *Phys. Rev. Lett*., **104**, 045001, (2010).
116. R. M. McDERMOTT et al., *Phys. Plasmas*, **16**, 056103, (2009).
117. D. G. WHYTE et al., *Nucl. Fusion*, **50,** 105005, (2010).
118. A. E. HUBBARD et al., *Nucl. Fusion*, **52,** 114009, (2012).
119. F. RYTER et al., 2011 38th EPS Conf. on Plasma Physics (Strasbourg, France, June 2011) vol 35G (ECA) P5.112 (2011).
120. J.W. HUGHES et al. Nucl. Fusion, **53**, 043016, (2013).
121. A. E. HUBBARD et al., "Progress in performance and understanding of steady-state ELM-free I-modes on Alcator C-Mod, 24th IAEA Fusion Energy Conference (2012) paper EX/1-3] (2012).
122. M. GREENWALD et al., *Phys. Plasmas*, 6, 1943, (1999).
123. Y. KAMADA et al., *Plasma Phys. Control. Fusion*, **42**, A247, (2000).
124. R. MAINGI, *Phys. Plasmas*, **13**, 092510, (2006).
125. N. OYAMA et al., *Nucl. Fusion*, **45**, 871, (2005).
126. E. J. DOYLE et al., *Phys Fluids*, **B3**, 2300, (1991).
127. P. T. LANG et al., *Nucl. Fusion*, **45**, 502, (2005).
128. L. R. BAYLOR et al., *Phys. Rev. Lett*., **110**, 245001, (2013).
129. A. D. TURNBULL et al., *Phys. Plasmas,* **6,** 1113, (1999).
130. L. L. LAO et al., *Nucl. Fusion*, **41**, 295, (2001).
131. A. D. TURNBULL et al., *Plasma Phys. Control. Fusion*, **45**, 1845, (2003).
132. T. E. EVANS, *J Nucl Mat*, **438**, S11, (2013).
133. P. T. LANG et al, *Phys Rev Lett*, **79**, 1478, (1997).
134. L. R. BAYLOR et al., *Phys Plasmas*, **7**, 1878, (2000).
135. L. R. BAYLOR et al., *Nuc Fusion*, **47**, 443, (2007).
136. A. S. KUKUSHKIN et al., *J Nucl Mat*, **415**, S497, (2011).
137. R. J. GROEBNER et al, *Nucl Fusion*, **44**, 204, (2004).
138. D. REITER, G. H. WOLF, and H. KEVER, *Nucl Fusion*, **30**, 2141, (1990).
139. M. R. WADE et al., *Phys Plasmas*, **2**, 2357, (1995).
140. A. SAKASAI et al., *J Nucl Mat*, **266-269**, 312, (1999).
141. A. SAKASAI et al., *J Nucl Mat*, **290-293**, 957, (2001).
142. H. TAKENAGA et al., *Fus Sci Tech*, **42**, 327, (2002).
143. K-D. ZASTROW et al., *Nucl Fusion*, **45**, 163, (2005).
144. G. W. PACHER et al., *Nucl Fusion*, **43**, 188, (2003).
145. G. W. PACHER et al., *Nucl Fusion*, **48**, 105003, (2008).
146. H. D. PACHER et al., *J Nuc Mat*, **313-316**, 657, (2003).

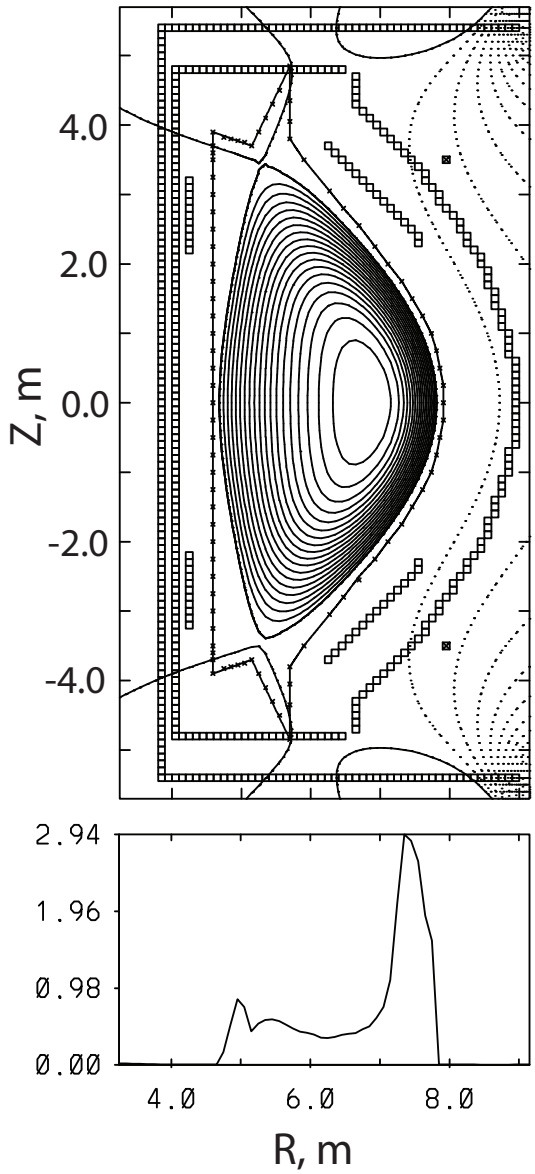

Figure 1. Plasma poloidal magnetic flux surfaces inside the conducting structure model including the vacuum vessel (outermost), ring structure (middle), tungsten stabilizer

plates (innermost), and feedback control coils for vertical position control. The limiter contour is used in the simulations, but may not adhere precisely to the final engineering design.

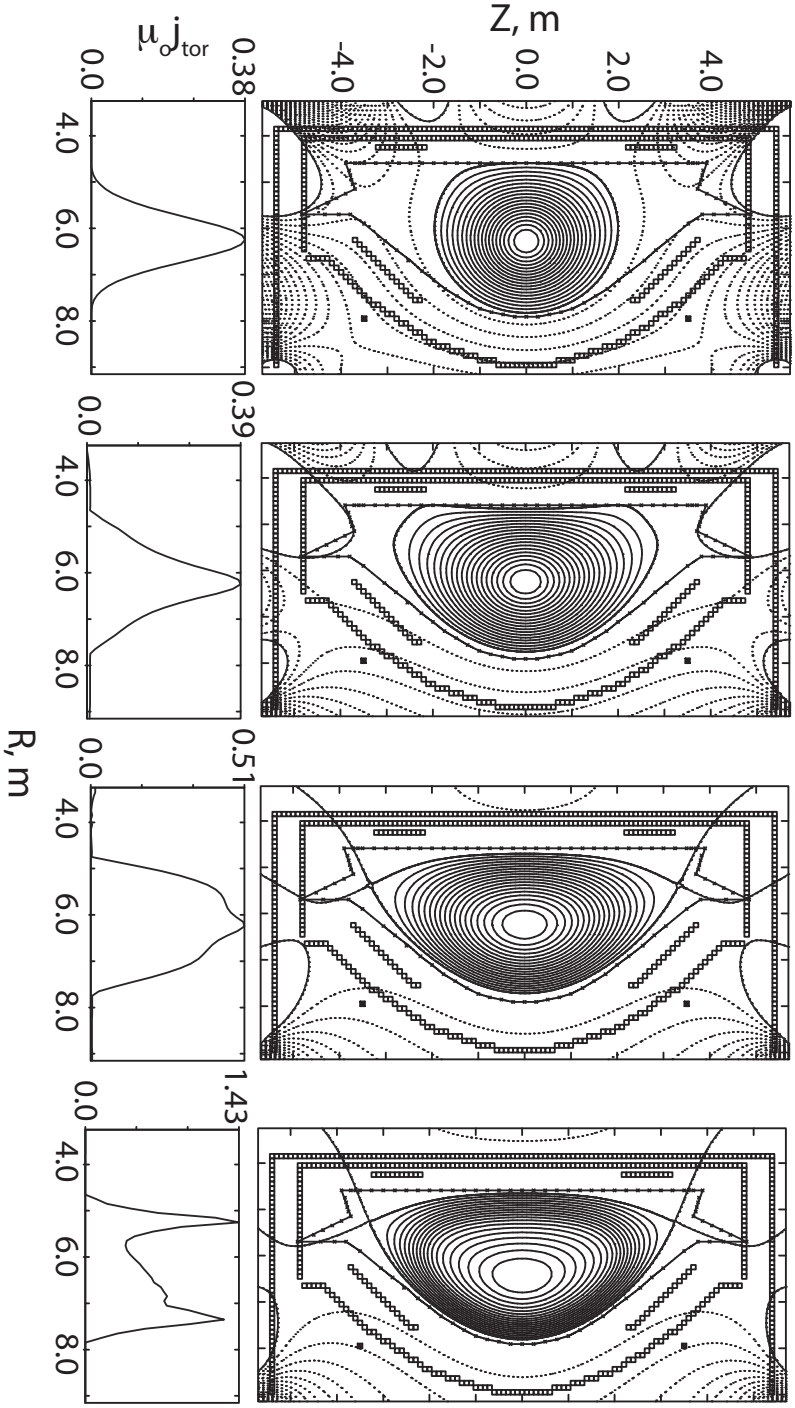

Figure 2. Poloidal magnetic flux surfaces during the growth phase and current rampup, 1.5 s, 3.4 s, 17.3 s, and 68.0 s. The plasma is limited until ~ 10 s, and 10 MW of power is injected at 15 s.

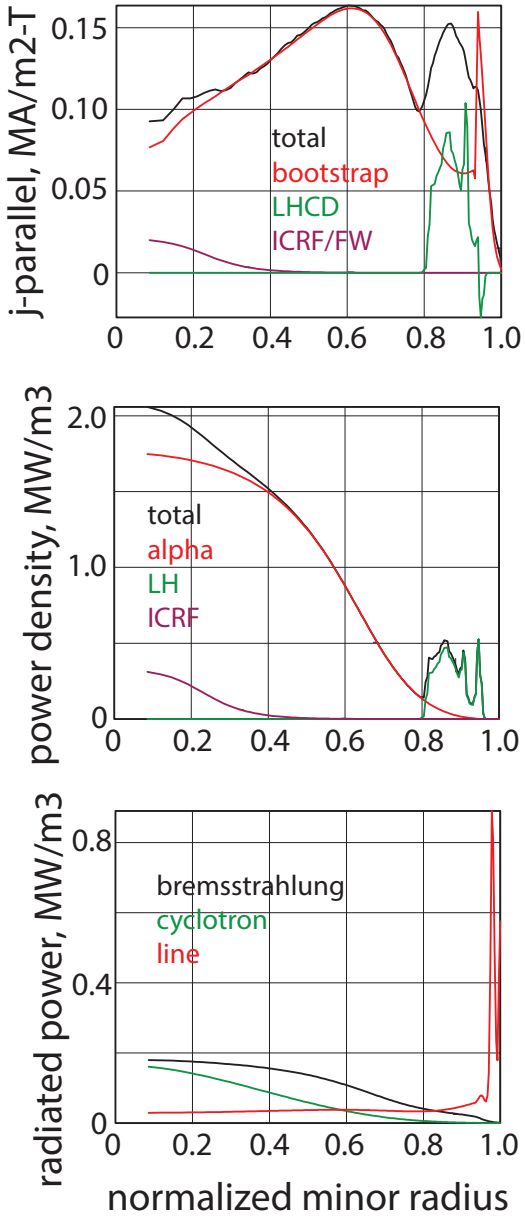

Figure 3. Profiles of parallel current density (total, bootstrap, LHCD and ICRF/FW), heating power densities (total, alpha, ICRF, and LH), and radiated power densities

(bremsstrahlung, cyclotron, and line) for the reference broad pressure profile case. Other profiles for the broad pressure case are shown in Fig. 6.

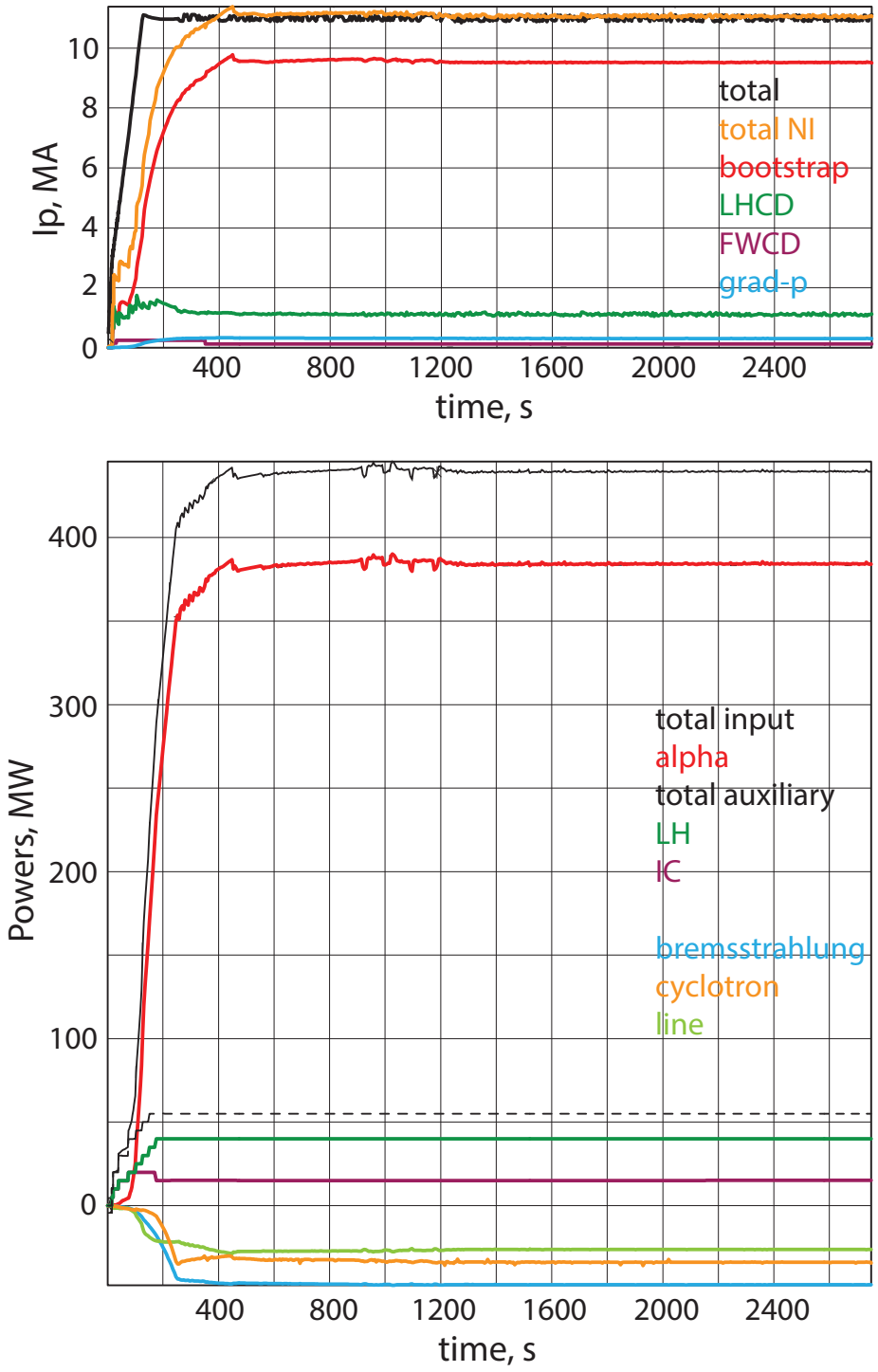

Figure 4. Time histories for ARIES-ACT1 discharge through to 2750 s, showing the plasma current contributions from bootstrap, LHCD, and IC FWCD. The contributions to the input powers in the plasma from alphas, LH, IC, and radiative losses from

bremsstrahlung, cyclotron and line terms. These are for the reference broad pressure case.

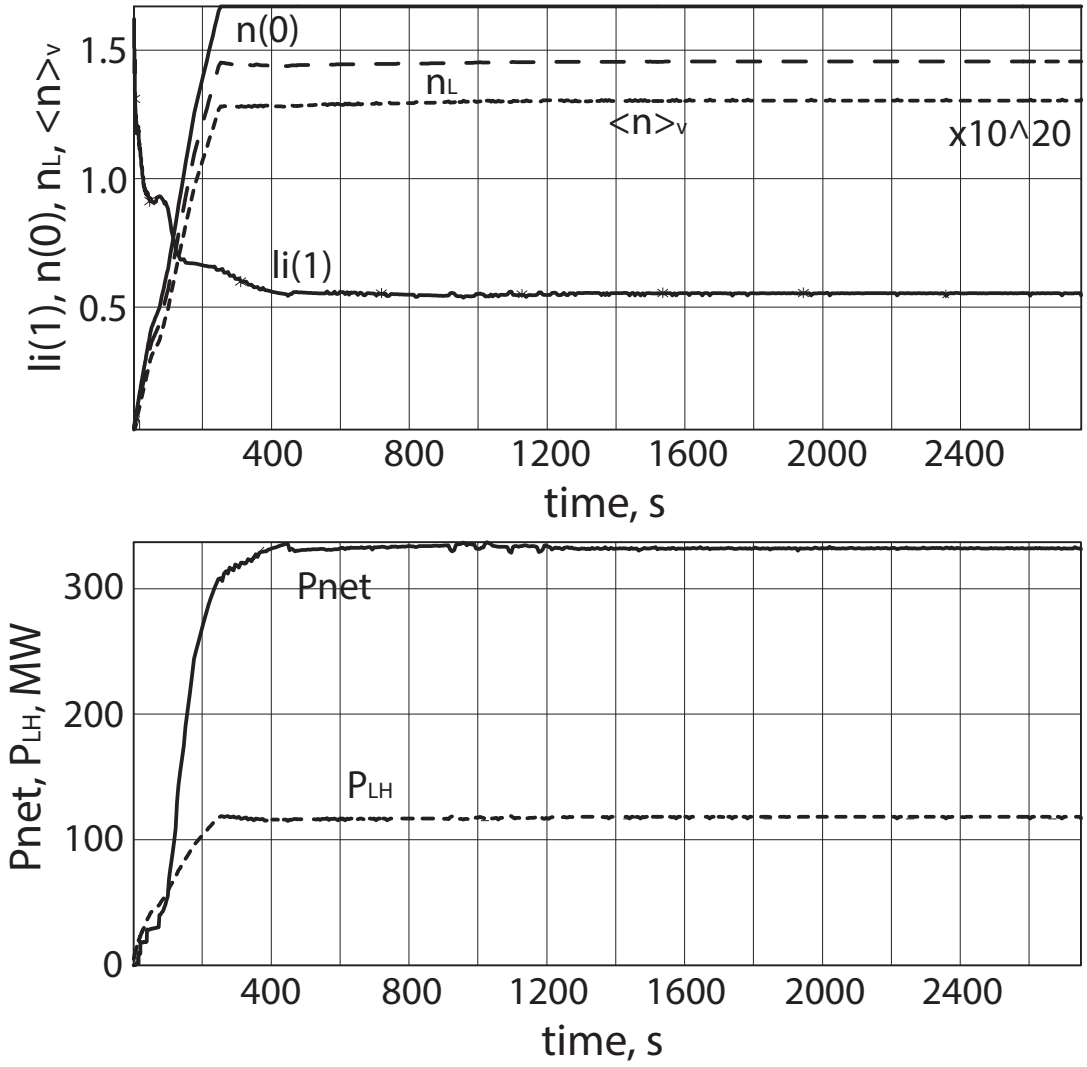

Figure 5. Time histories of the plasma density, internal self-inductance li(1), net power to the plasma ($P_{alpha}+P_{aux}-P_{rad,core}-dW/dt$), and threshold power for the L to H transition. These are for the reference broad pressure case.

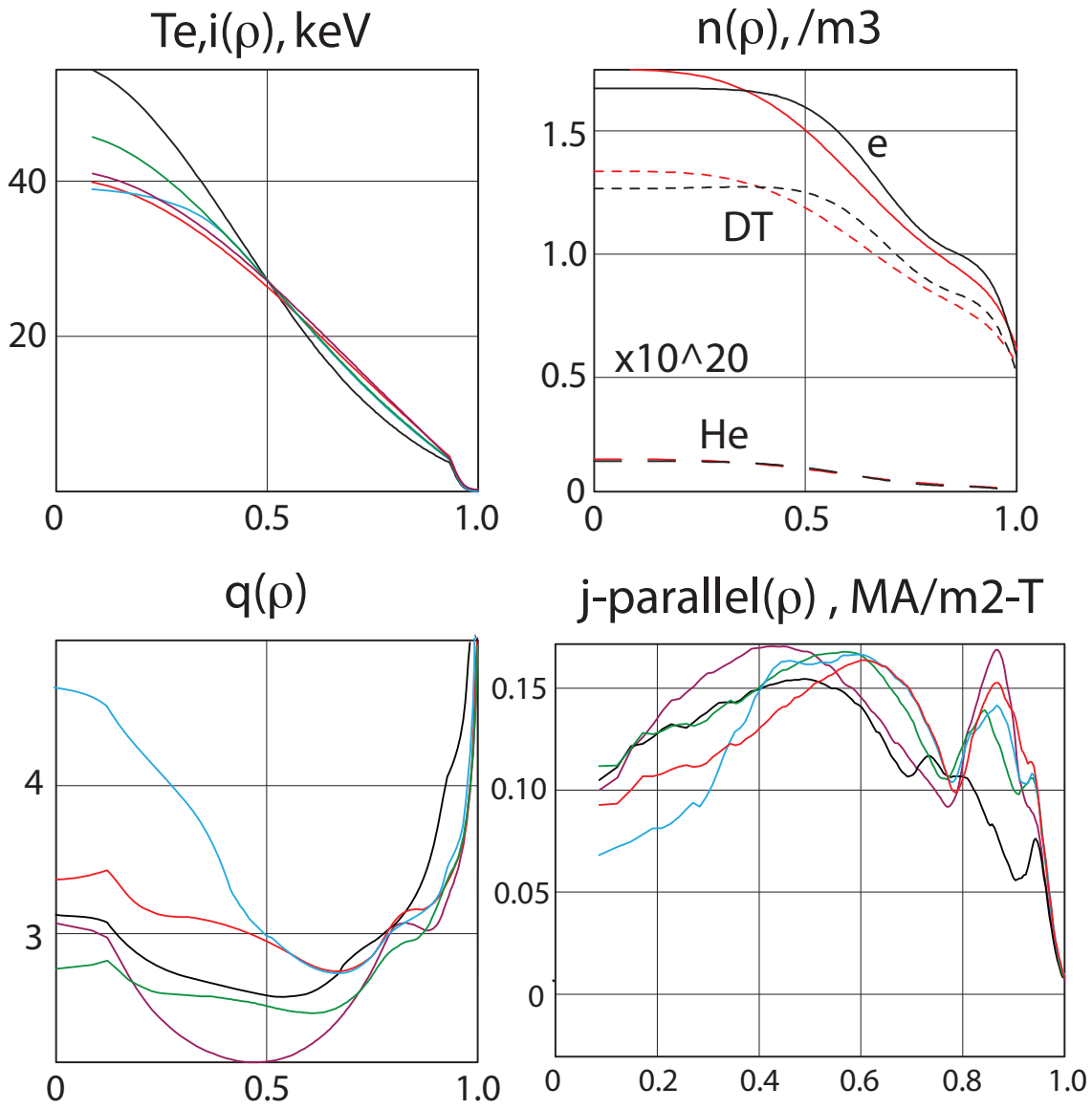

Figure 6. Profiles of the electron temperature, electron density and safety factor profiles when relaxed for the 1) broad pressure (red), 2) broad pressure 2 (blue), 3) medium pressure(green), 4) peaked pressure (black), 5) and density (purple) with broad pressure cases. The density profiles shown are the reference (black) and the more distributed gradient profile (red) used in the density-broad pressure case.

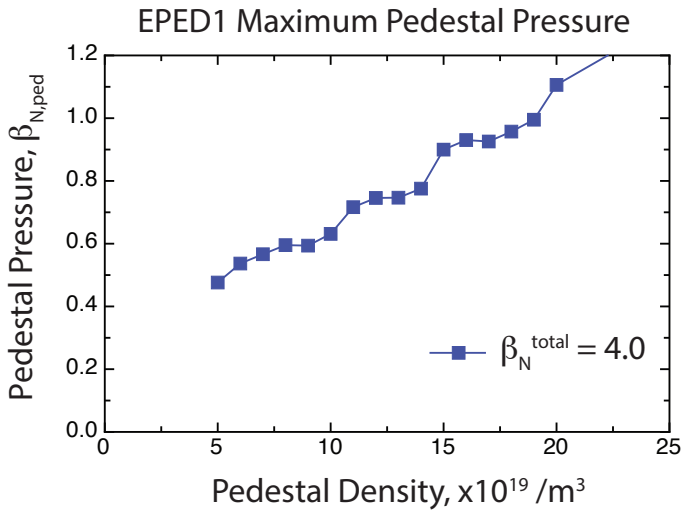

Figure 7. The peeling ballooning stability analysis from EPED1, for the maximum pedestal pressure as a function of the pedestal electron density, showing the improvement with increasing density. The reference pedestal density is 0.9-1.0x10^{20} /m^3 for ACT1, giving a β_{Nped} of 0.6, or a maximum pedestal temperature of ~ 3.75-4.25 keV.

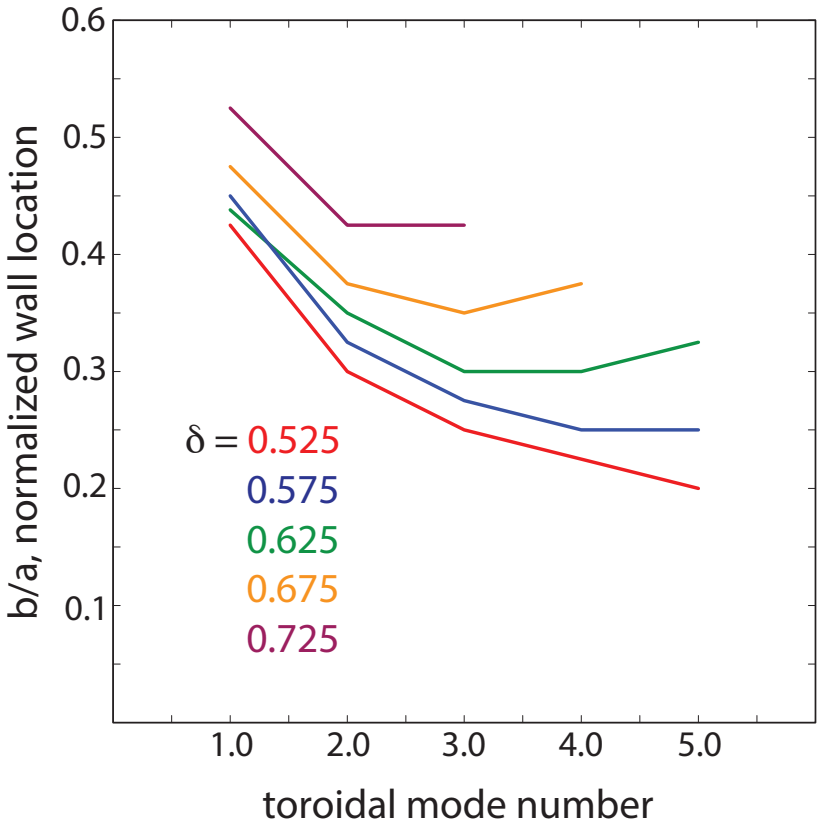

Figure 8. The ideal MHD stability for low-n kink modes, n = 1-5, as a function of the plasma triangularity, to determine the minimum stabilizing wall location for the broad pressure configuration at a total $\beta_N = 5.72$. The plasma elongation is fixed at 2.2 at the x-point. The reference traingularity is 0.625, requiring a conducting wall on the outboard side of the plasma at 0.3 times the minor radius measured from the plasma boundary.

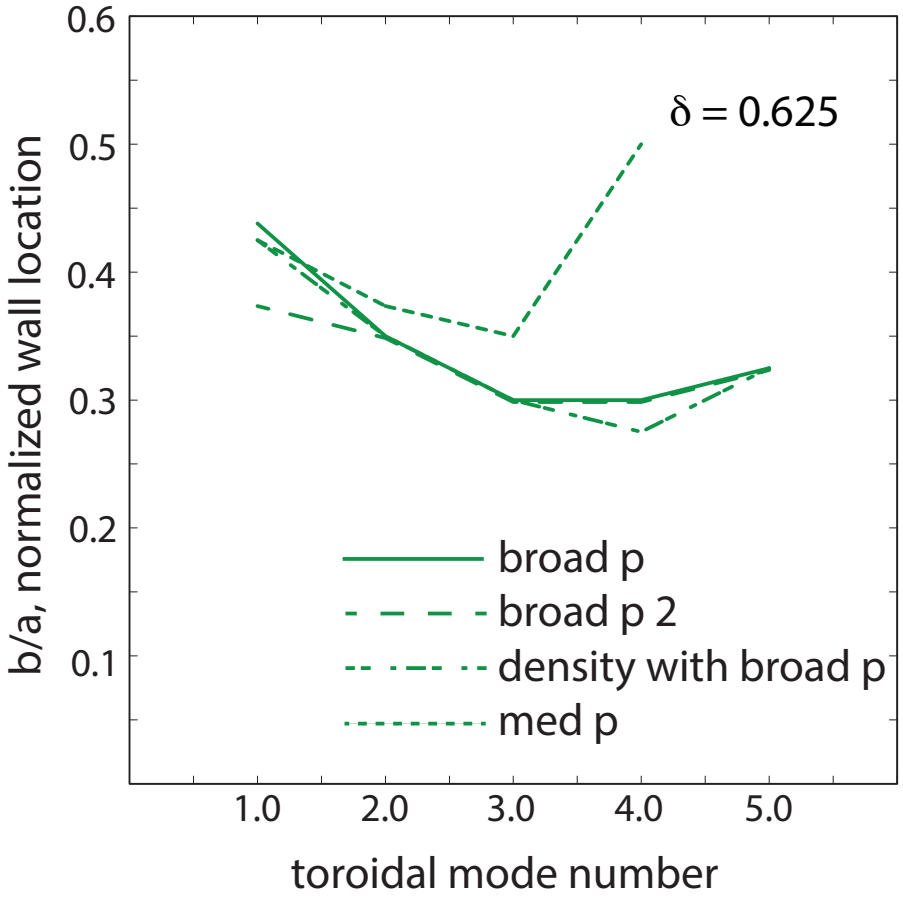

Figure 9. The ideal MHD stability for low-n kink modes, n = 1-5, with the reference triangularity, for the various plasma configurations at their corresponding normalized betas.

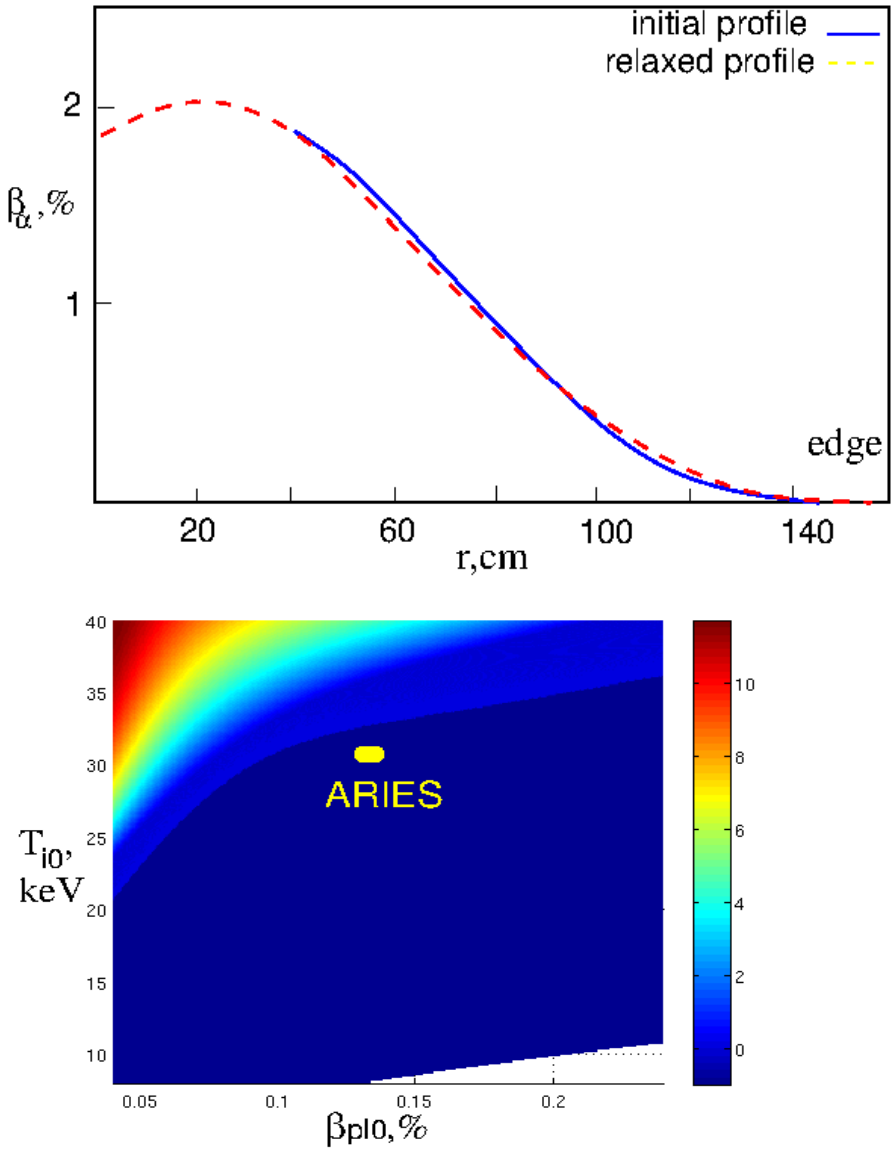

Figure 10. The top figure represents the initial alphas beta profile (blue solid curve) and the relaxed profile (yellow dashed curve) obtained by the 1.5D model application. The bottom figure shows the T_i-β_{p0} diagram with the operational point of the ARIES plasma and the color-coded expected losses of alphas as predicted by the 1.5D model. The analyses shows that the ARIES-ACT1 operational point is outside of the predicted loss region.

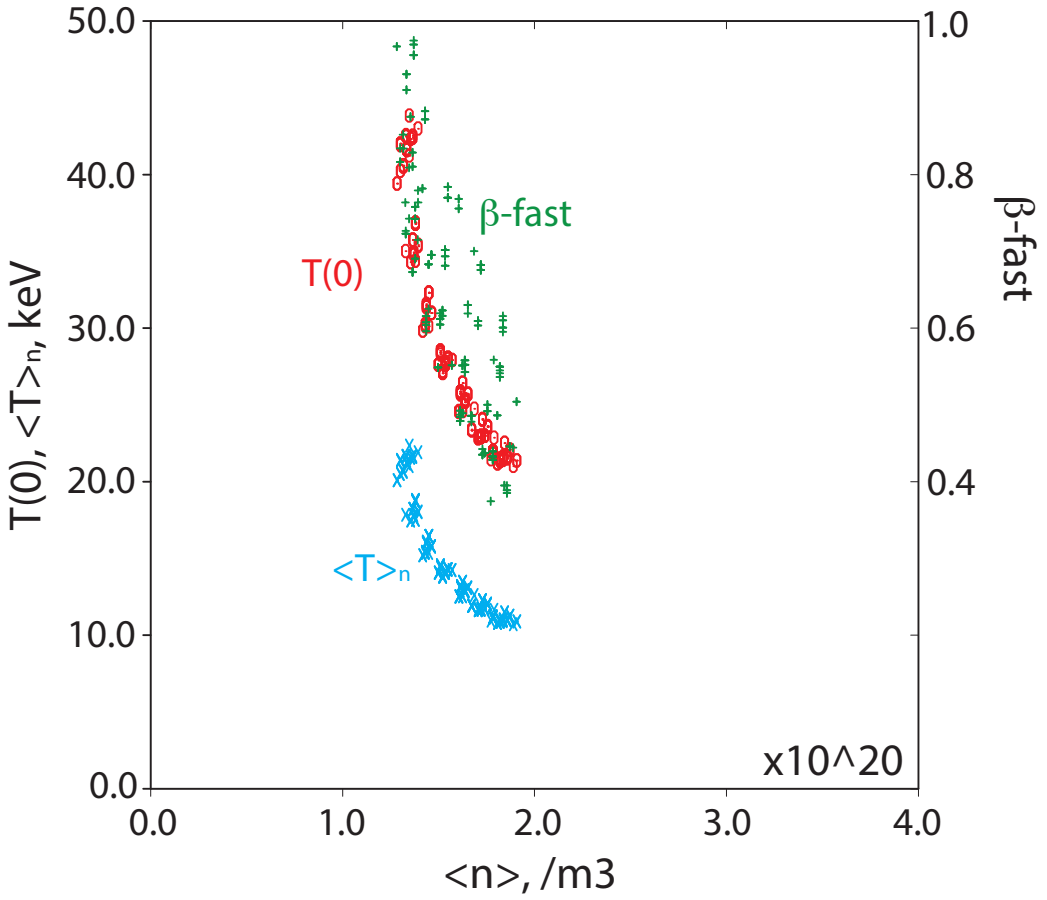

Figure 11. Results of systems code scan of plasmas producing 1000 MW_e, with R = 6.25 m, as the density is increased making n/n_{Gr} vary from 1.0 to 1.6. The increase in density has resulted in a strong reduction in the central and density weighted volume average temperatures, as well as the fast particle beta. Plasma configurations at or above the Greenwald density is a common result for power plants.

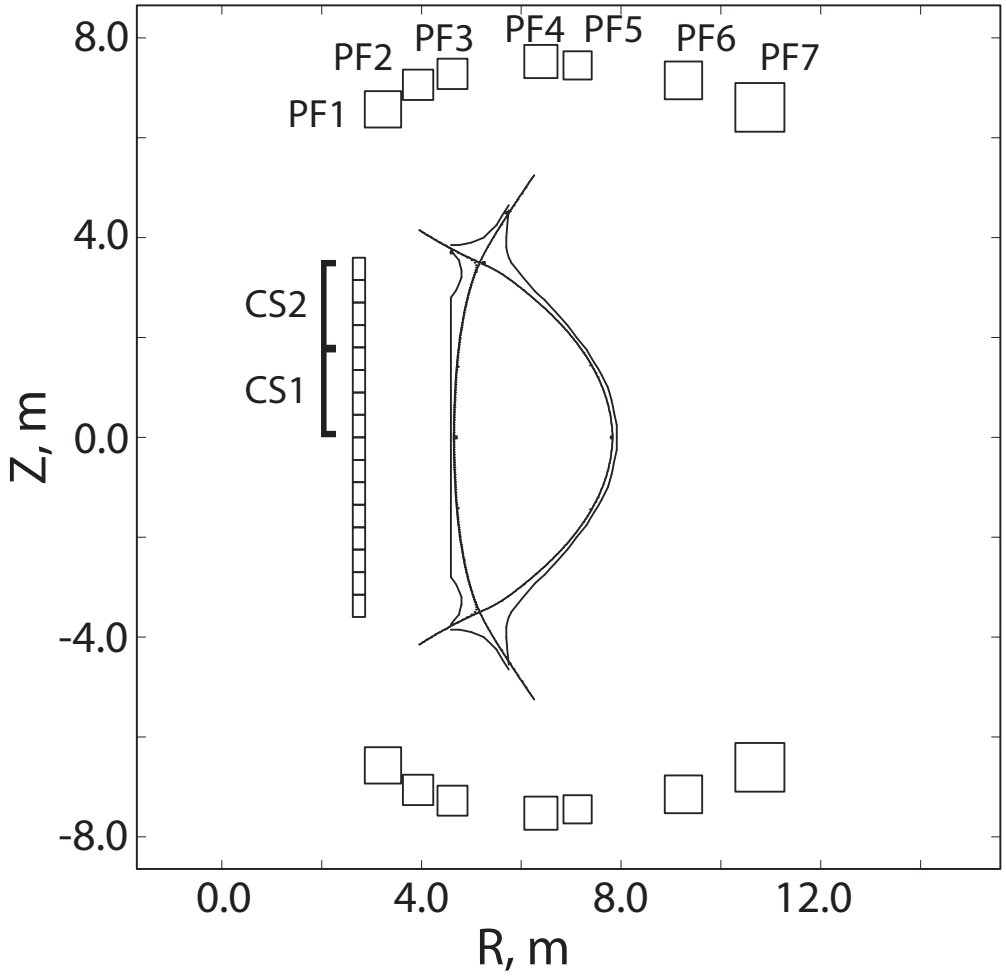

Figure 12. Layout of the final poloidal field coils, with central solenoid (CS) and outer poloidal field (PF) coils. The locations are determined by available space outside the TF coil support structure and the vacuum vessel port extensions.

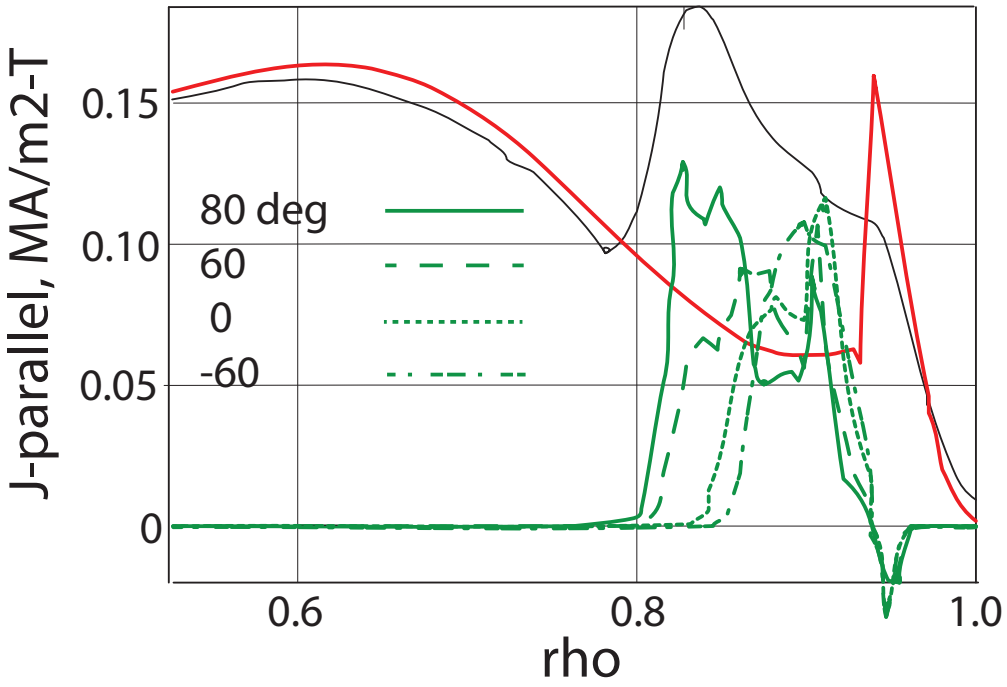

Figure 13. Parallel current densities of lower hybrid current drive with different launching locations (green curves), the poloidal angle is measured relative to the outboard midplane, from the plasma geometric center (R=6.25, Z=0). The parallel index is the same for all cases at 2.15, and the red curve shows a typical bootstrap and the black curve is a typical total current density. The above-midplane locations lead to higher driven current and deeper penetration.

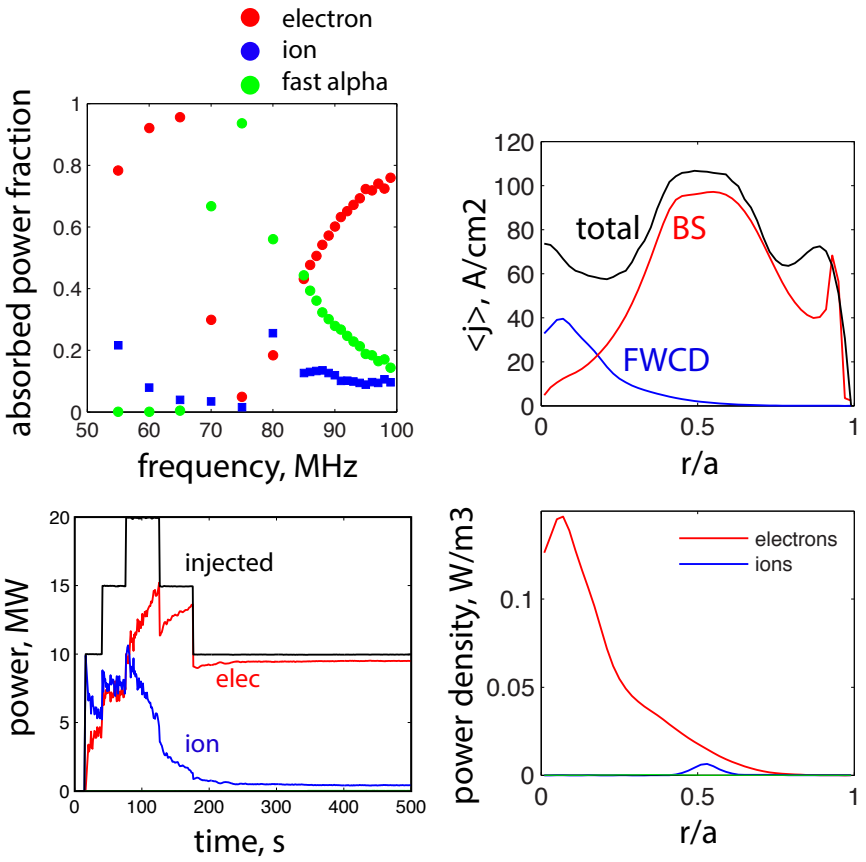

Figure 14. Analysis of the ICRF system for ARIES ACT1, shows that the electron absorption is maximized around 65 MHz shown in the absorbed power versus frequency plot. The power deposition and driven current profiles are shown for this frequency in the relaxed flattop phase. The power absorbed on thermal ions and electrons is also shown as a function of time, indicating the competitive ion heating over the first 100s, as opposed to the dominant electron heating later.

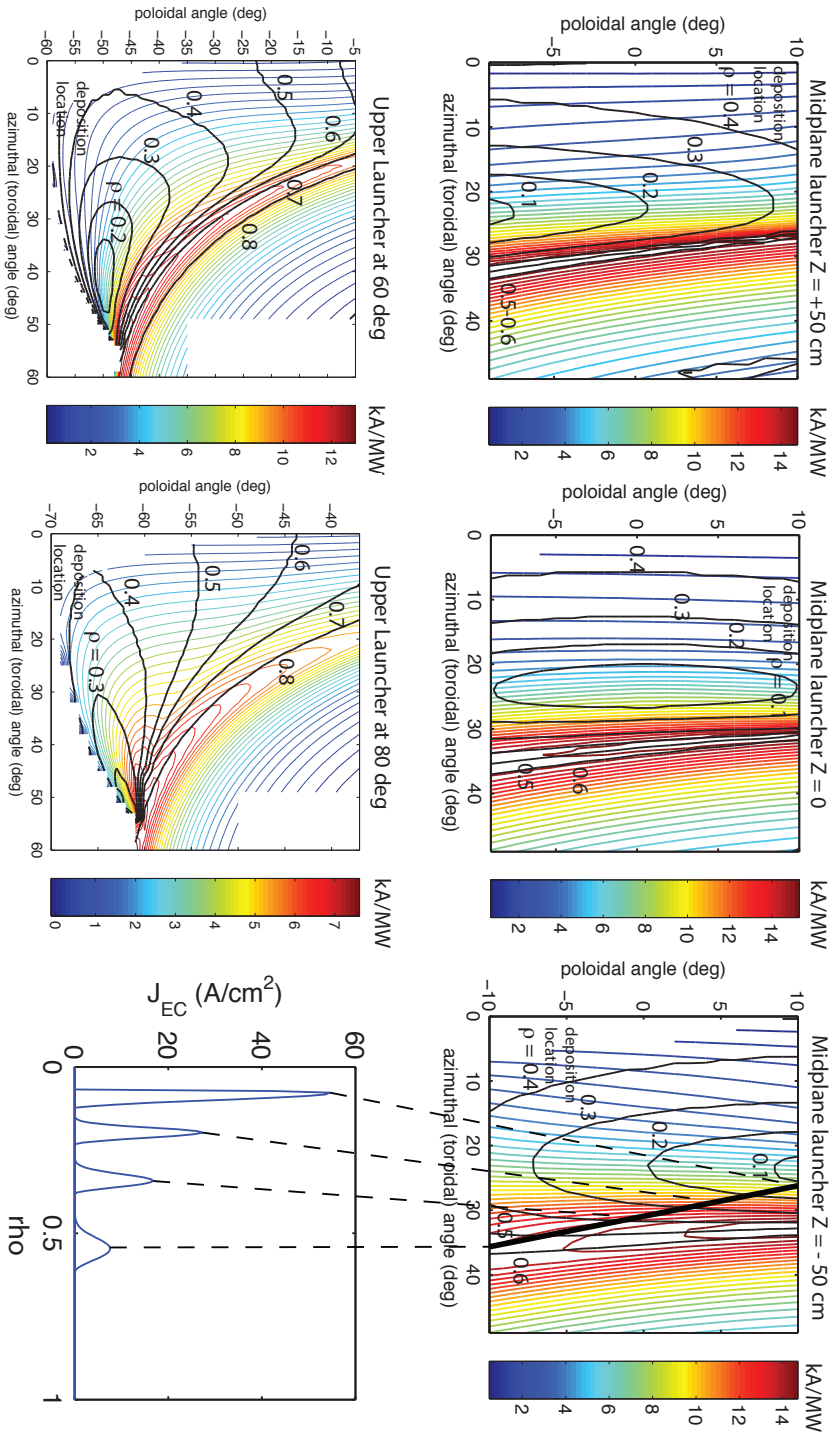

Figure 15. The current drive efficiency using electron cyclotron launched from 5 locations, 3 near the midplane and 2 above the midplane at 60 and 80 deg. The curves show the contours of deposition location in normalized minor radius and the kA/MW driven, for the combination of poloidal and toroidal steering angles. Also shown are the current density profiles for a few cases demonstrating the range of deposition locations.

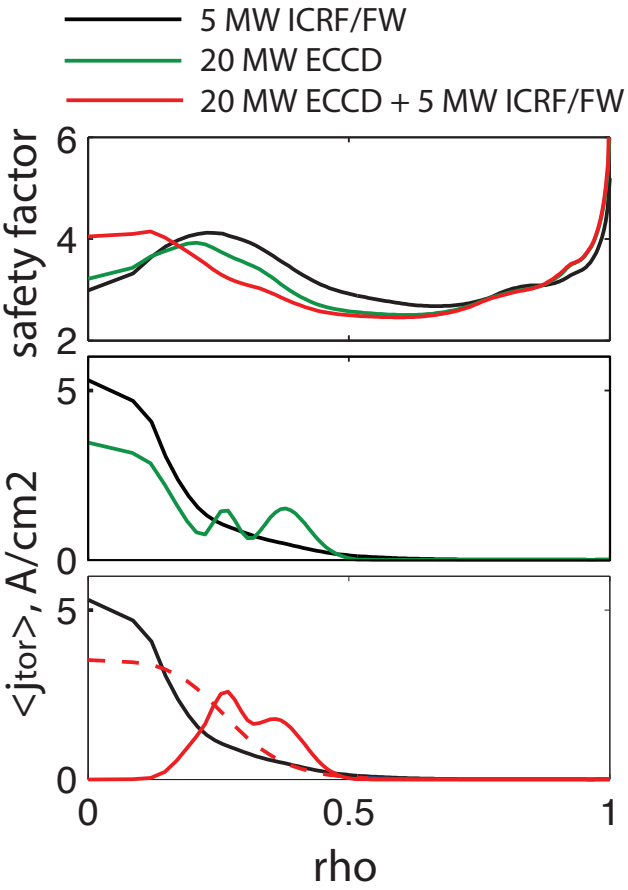

Figure 16. Safety factor and current density profiles for the reference case with 40 MW of LH and 5 MW of IC, a case with the 5 MW of IC replaced with 20 MW of EC, and a case with the 5 MW of IC and 20 MW of EC added to it. The resulting safety factor profile changes can be seen, demonstrating the deposition range of the EC.

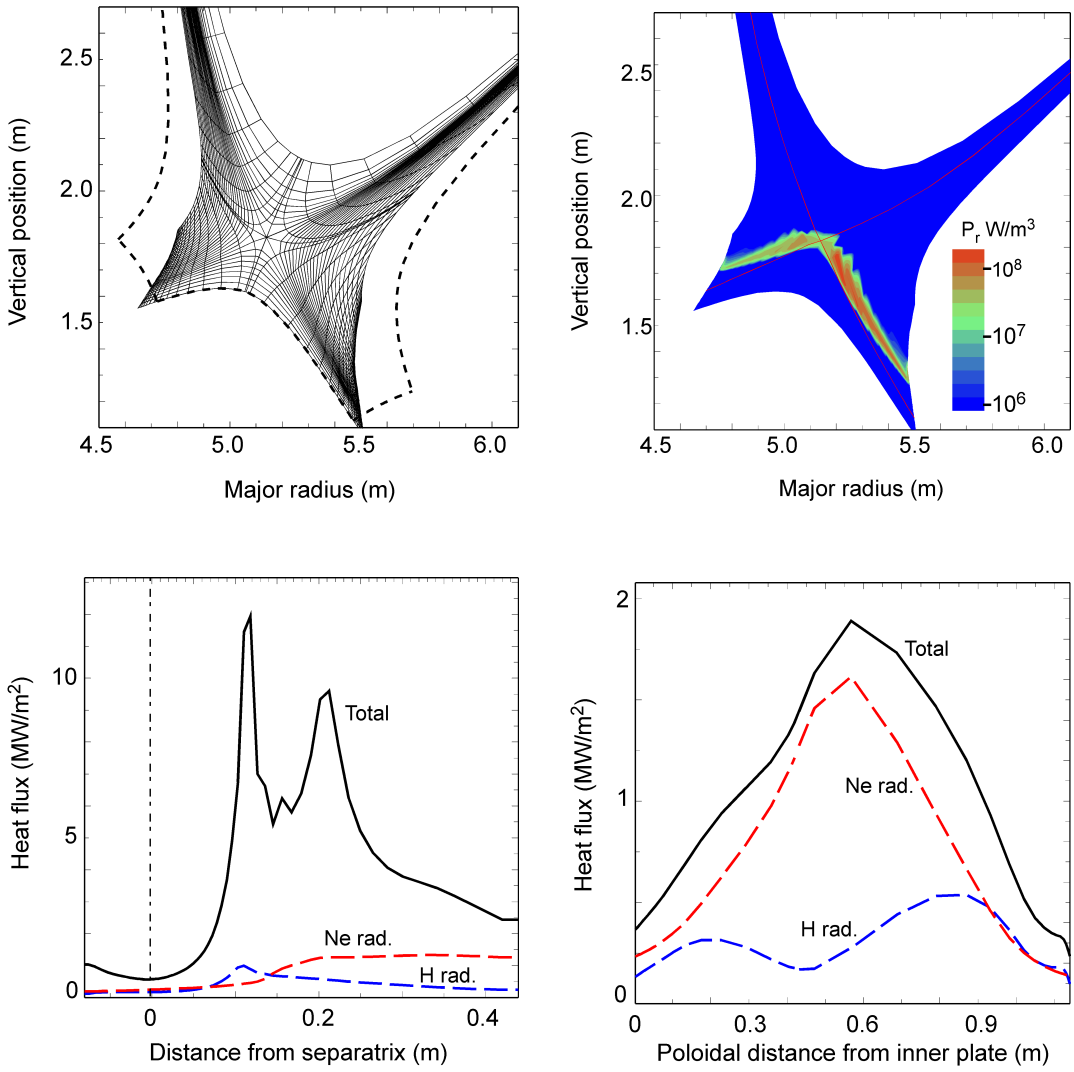

Figure 17. Lower divertor region of computational mesh for the tilted-plate divertor configuration (upper left). Compared to the simulation, the number of radial mesh points is reduced here by ½ for clarity. The dashed line represents the domain for the fully-detached divertor configuration. Neon radiation contours for tilted-plate case (upper right). Total heat-flux along the outer divertor plate and individual contributions from neon and hydrogenic radiation (lower left). Total heat-flux along the private-flux boundary (bottom of grid region) with dominant radiation components (lower right).

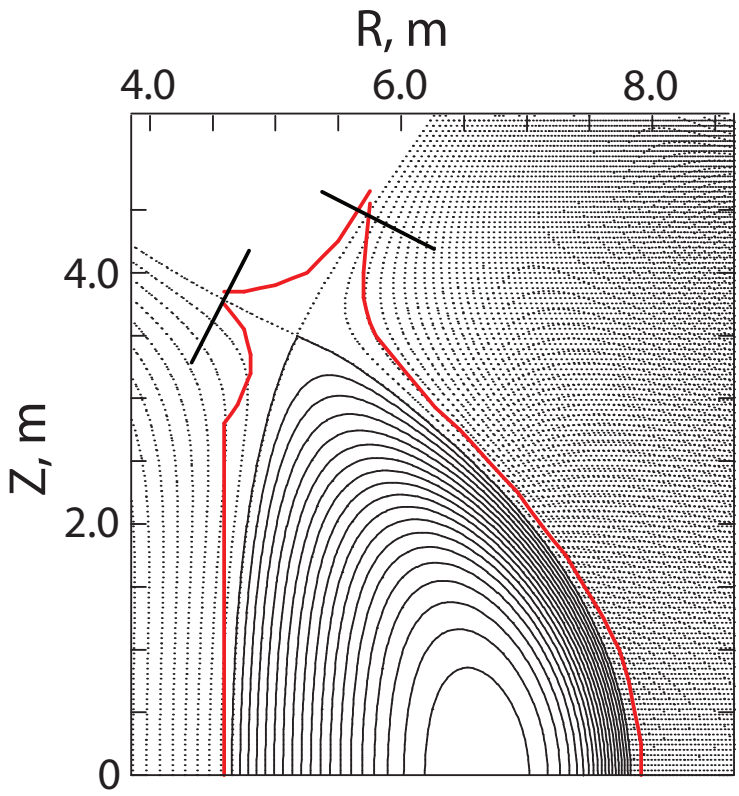

Figure 18. Poloidal flux contours for the ARIES-ACT1 plasma and regions outside the last closed flux surface. The approximate divertor shape is provided to show the flux angles and expansion.

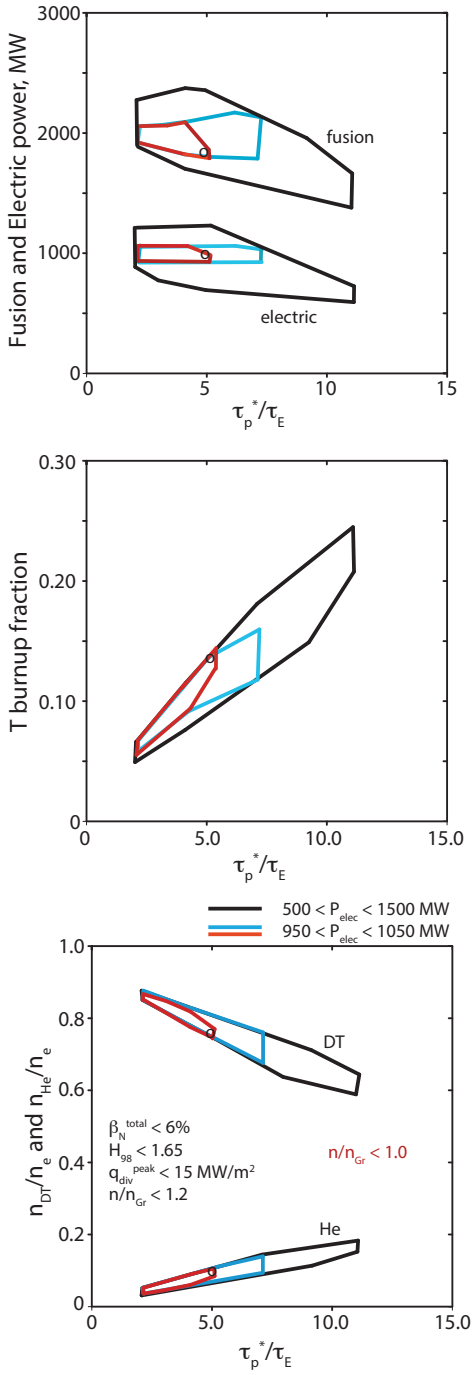

Figure 19. Systems analysis determination of variation in operating points as the ratio of global particle confinement time to global energy confinement changes, based on ARIES-ACT1 plasma geometry, toroidal field, q_{95}, impurity fraction, and current drive efficiency. The viable solutions exist inside the contours, and the ARIES-ACT1 operating point is shown by the black circle.

The Princeton Plasma Physics Laboratory is operated
by Princeton University under contract
with the U.S. Department of Energy.

Information Services
Princeton Plasma Physics Laboratory
P.O. Box 451
Princeton, NJ 08543

Phone: 609-243-2245
Fax: 609-243-2751
e-mail: pppl_info@pppl.gov
Internet Address: http://www.pppl.gov